Cosmogenic (un-)steadiness revealed by paired-nuclide catchment-wide denudation rates in the formerly half-glaciated Vosges Mountains (NE France)

Timothée Jautzy, Gilles Rixhon, Régis Braucher, Romain Delunel, Pierre G Valla, Laurent Schmitt

To cite this version:

Timothée Jautzy, Gilles Rixhon, Régis Braucher, Romain Delunel, Pierre G Valla, et al.. Cosmogenic (un-)steadiness revealed by paired-nuclide catchment-wide denudation rates in the formerly half-glaciated Vosges Mountains (NE France). Earth and Planetary Science Letters, 2024, 625, pp.118490. 10.1016/j.epsl.2023.118490 . hal-04294607

HAL Id: hal-04294607

https://hal.science/hal-04294607

Submitted on 21 Nov 2023

Cosmogenic (un-)steadiness revealed by paired-nuclide catchment-wide denudation rates in the formerly half-glaciated Vosges Mountains (NE France)

Timothée Jautzy[1], Gilles Rixhon[1,2], Régis Braucher[3], Romain Delunel[4], Pierre G. Valla[5], Laurent Schmitt[1], ASTER Team[3]

[1]Laboratoire Image Ville Environnement - CNRS - UMR7362, Université de Strasbourg, Strasbourg, France

[2]Ecole Nationale du Génie de l'Eau et de l'Environnement de Strasbourg (ENGEES), Strasbourg, France

[3]Aix-Marseille Univ., CNRS-IRD-INRAE-Collège de France, UM 34 CEREGE, Technopôle de l'Environnement Arbois-Méditerranée, BP80, 13545 Aix-en-Provence, France

[4]Univ Lyon, Université Lumière Lyon 2, CNRS, UMR 5600 EVS, F-69635

[5]Institute of Earth Sciences (ISTerre), Université Grenoble Alpes, Université Savoie Mont Blanc, CNRS, IRD, IFSTAR, 38000, Grenoble, France

Keywords: 10Be-26Al; Catchment-wide denudation rates; Vosges Massif; Impact of former glaciations; Cosmogenic disequilibrium

Abstract

Although catchment-wide denudation rates inferred from *in situ* cosmogenic nuclide concentrations measured in stream sediments has represented a ground-breaking progress in geomorphology over the last three decades, most of these studies rely on ^{10}Be concentrations only. It seems that this current and routine one-nuclide approach to infer catchment-wide denudation rates has somehow overshadowed two key assumptions that are cosmogenic steady-state and short sediment transit time at the catchment scale. Although a paired-nuclide approach allow testing these assumptions, it is rarely performed on stream sediments and this can become highly problematic in slow-eroding, formerly glaciated contexts. In this study, we thus measure both ^{10}Be and ^{26}Al in stream sediments pertaining to twenty-one rivers draining an entire low mountain range: the Vosges Massif (NE France). The latter exhibits a sharp gradient between its southern and northern part in terms of lithology, morphometry and climate. Moreover, if its northern part remained void of glacial cover during Quaternary cold stages, its southern part was significantly and repeatedly glaciated. We aim to assess the factors that control the denudation of the Vosges Mountains and to quantitatively explore the impact of both repeated glacial cover and storage of glacially derived sediments on ^{26}Al/^{10}Be ratios, hence cosmogenic (un-)steadiness in modern river samples. Our results first show that elevation, slope, channel steepness and precipitation are primarily organised along a N-S increasing trend. ^{10}Be- and ^{26}Al-derived catchment-wide denudation rates accordingly range from 34±1 to 66±2, and 41±3 to 73±7 mm/ka, respectively, in thirteen investigated catchments that are in cosmogenic equilibrium. Lithological contrasts

may control the pattern of denudation with a higher erodibility of the sandstone-dominated catchment to the north compared to the crystalline-dominated catchments to the south.

Our results also show that catchments in strong cosmogenic disequilibrium (^{26}Al/^{10}Be ratios from 1.4 to 5.2) spatially cluster in the SW part of the Vosges Mountains that was the most intensively glaciated during Quaternary cold stages. If this precludes any conclusion about controlling factors at the whole massif scale, this study is the first to quantify the impact of past glaciations on cosmogenic (un-)steadiness measured in stream sediments. A statistically significant relationship between the degree of depletion of the ^{26}Al/^{10}Be ratios and the spatial pattern of glaciation is found: the larger the former glacial cover in each catchment, the lower the ^{26}Al/^{10}Be ratio. Equally important is the significant correlation reported between the degree of depletion of the ^{26}Al/^{10}Be ratios and the proportion of glacial and fluvio-glacial deposits within each catchment. These two relationships underline the link between cosmogenic unsteadiness in the stream cosmogenic signal and long-lasting and repetitive ice shielding, and complex sediment routing systems in glacial environments, respectively. We thus argue to systematically measure ^{26}Al in complement to ^{10}Be and to test the steady-state assumption when it comes to infer catchment-wide denudation rates from modern stream sediments, especially in slow eroding, formerly glaciated landscapes.

1. Introduction

Assessment of catchment-wide denudation (CWD) rates inferred from *in situ* cosmogenic nuclide concentrations measured in modern stream sediments has represented a ground-breaking progress in geomorphology over the last three decades (von Blanckenburg, 2005; Dunai, 2010; Granger and Schaller, 2014). This approach has been applied to fluvial catchments from practically every tectonic and climatic setting worldwide, including currently (e.g. Grin et al., 2018) and formerly (e.g. Buechi et al., 2014) glaciated terrains. The key research aim of those studies consists in disentangling the complex interplays between topography (e.g. Peifer et al., 2021), tectonics (e.g. Olivetti et al., 2016), climate (e.g. Carretier et al., 2013) and lithology (e.g. Cyr et al., 2014) which primarily control denudation. The thousands of river-sediment samples collected in the majority of case studies, however, were processed to measure *in situ* ^{10}Be concentrations only (Portenga and Bierman, 2011). Although this single-nuclide approach relies on several key assumptions, it seems that the current ^{10}Be's routine approach used to infer CWD rates has somehow overshadowed two of them. First, little attention has been recently paid to cosmogenic steady-state at the catchment-scale (von Blanckenburg, 2005). It implies that the catchment's inbound flux via ^{10}Be production is counterbalanced by the outbound flux by denudation and decay at the catchment's outlet where the sampling takes place. Second, the timespan over which sediments are transported within the catchment to the outlet, i.e. sediment transit time, must be short compared to the timespan over which denudation occurs (Dunai, 2010). In settings where these conditions might not be met, ^{10}Be radioactive decay can become sizeable so that special care must be taken in settings where long-term sediment storage and remobilisation is evidenced. Neither the assumption of catchment's steady-state nor that of short sediment transit time can be checked by processing river-sand ^{10}Be concentrations only. As for steady-state, glacier cover, glacial erosion and/or glacially derived sediments may significantly impact the estimation of ^{10}Be-derived CWD rates in currently (e.g. Delunel et al., 2014) or formerly (e.g. Glotzbach et al., 2013) glaciated catchments. As for transit time, glacial and post-glacial environments have complex sediment routing systems (e.g. Porter et al., 2019) where reworking of ancient sediments impacts cosmogenic inventories as well (e.g. Wittmann et al., 2009; Buechi et al., 2014). A few ^{10}Be-based studies developed some modelling approaches to partially cope with this twofold key issue (Godard et al., 2012; Glotzbach et al., 2013).

Examination of steady-state, transit time and potential storage are potentially better constrained by measuring both ^{10}Be and ^{26}Al concentrations in the same quartz-bearing sample (e.g. Bhattacharjee et al., 2023). Since its original formulation in Lal's (1991) paper, the two-nuclide diagram distinguishes those samples that meet the steady-state assumption by plotting in the so-called steady-erosion island (Dunai, 2010) from those that underwent complex exposure histories and are characterised by depleted ^{26}Al/^{10}Be ratios. This approach has been widely used in formerly glaciated regions of e.g. Greenland (Corbett et al., 2013; Strunk et al., 2017; Andersen et al., 2020) and Scandinavia (Andersen et al., 2018; Knudsen and Egholm, 2018) to successfully assess glacial erosion efficiency and denudation rates. Depleted ^{26}Al/^{10}Be ratios in many glacial bedrock and erratic samples clearly violate the steady-state assumption due to repeated and extensive burial under thick ice masses with low erosive potential, i.e. cold-based glaciers. On the contrary, the paired-nuclide (^{26}Al-^{10}Be) approach was only applied in few studies for modern stream sediments, although Wittmann et al. (2020) recently highlighted significantly depleted ^{26}Al/^{10}Be ratios in 35% of the >50 large rivers they studied all over the Earth's surface. Merely a handful of these studies dealt with glaciated catchments (Safran et al., 2005; Hippe et al., 2012; Grin et al., 2018; Wittmann et al., 2020; Zhang et al., 2021), but cosmogenic disequilibrium is highlighted not only in currently glaciated catchments of Tibet (Zhang et al., 2021) but also in formerly and marginally glaciated catchments of the Bolivian Andes (Hippe et al., 2012). However, Zhang et al. (2021) could only conclude that sediment reworking is a potential issue without further exploration nor quantification on this process. This altogether demonstrates our current lack of understanding in how cosmogenic signals measured in modern stream sediments might be perturbed in (formerly) glaciated catchments.

Located in north-eastern France, the Vosges Massif (or Vosges Mountains; VM) is a favourable setting to investigate this question. This S-N oriented low-elevation mountain range exhibits a sharp dissimilarity between its southern and northern part in terms of lithology, morphometry and climate. Topographic imprints from successive Quaternary glaciations in the VM landscape also follow this spatial pattern: whereas most of the crystalline southern VM were repeatedly covered and shaped by thick glaciers (Flageollet, 2002; Mercier, 2014), the northern half was void of ice cover (Darmois-Théobald, 1972; Heyman et al., 2013). Taking advantage of the VM setting and characteristics, this study aims at (i) demonstrating the spatial structuration of the VM in terms of first-order controlling factors for catchment-scale denudation, (ii) evaluating the cosmogenic (dis)equilibrium in the VM and (iii) quantitatively exploring the impact of both repeated glacial cover and storage of glacially derived sediments on paired cosmogenic ratios. First, morphometric and climatic indices are computed and groups of lithologically uniform catchments are statistically determined. Second, modern stream sediments from 21 river-catchments outlets draining the whole VM are sampled for *in situ* ^{10}Be and ^{26}Al concentration measurements. Third, a systematic comparison is undertaken between ^{26}Al/^{10}Be ratios and high-resolution data including previous glacial coverage, as well as the spatial distribution of glacial and fluvio-glacial sediments.

2. Study area

The VM form the western footwall block of the southern Upper Rhine Graben (north-eastern France; Fig. 1A). Its uplift is assigned to Miocene lithospheric folding resulting from NW-directed compressional stresses exerted in the Alpine foreland (e.g. Ziegler and Dèzes, 2007). Plio-Quaternary tectonic re-activation and uplift were assumed as well (Harmand and Cordier, 2012). The VM's lithology primarily is bipartite: Paleozoic crystalline rocks and Triassic sandstones compose the southern (~2/3) and northern (~1/3) parts, respectively (Fig. 1B). Strongly contrasting with the almost uniform Mesozoic sedimentary cover to the north, the Paleozoic basement reaches Hercynian orogenic units with various lithologies (Fig. 1B; Skrzypek, 2011). Plutonic rocks prevail (i.e. granites and (grano-)diorites mostly) but metamorphic (i.e. mostly gneiss) and volcanic (i.e. various lavas and tuffs) rocks also occur.

The VM exhibit a well-marked N-S topographic gradient, from a low- to medium-elevation mountain range from north to south. Mean and peak elevations along three WNW-ESE oriented swath profiles performed in the VM's northern, central and southern parts amount to ~255/525, 470/1090 and 710/1350 m asl, respectively (Fig. 2A). A southward massif-scale increasing trend in normalised channel steepness index reflects this gradient as well (Fig. 1C). The VM is sharply bounded by the Vosgian normal fault system bordering the Upper Rhine Graben whereas its western side falls upon the slightly tilted Mesozoic formations from the Paris Basin (Figs. 1, 2A). Owing to the NNE/SSW-orientation of its main topographic divide, the VM typically form an almost perpendicular orogenic barrier to the predominant oceanic western atmospheric flow, thereby inducing a typical rain shadow effect (Fig. 1D; François and Humbert, 2000). Mean annual rainfall concomitantly increases with elevation along the main ridge as well, ranging from about 900 mm/a in the northern part to up to 1400 mm/a at elevations higher than 1350 m (Fig. 1D). Deciduous, resinous and mixed forests cover no less than ~70% of the VM's area (Rochel, 2004). They essentially occur on hillslopes and plateau-top positions, regardless the geographic location within the massif (except the bare, highest interfluves in the southern part; Fig. 2Bc).

The spatial pattern of Quaternary glaciations and their imprints on the landscape reflect this massif-scale dichotomy (Fig. 1E; Flageollet, 2002; Mercier & Jeser, 2004; Mercier, 2014). To the north, roughly two thirds of the VM exhibit fluvially overprinted landscapes (Fig. 2Ba-b). They completely lack evidence of former glacial activity and allow inferring an ice-free area in the northern third of the VM (Flageollet, 2002). Fluvial landscapes of the central part bear witness of local and sparse evidence of low-magnitude past glacial activity, i.e. small-dimensioned cirques and cirque moraines (Darmois-Théobald, 1972; Fig. 1E). Whilst mean fluvial incision usually ranges from ~150 (Fig. 2Ba) to 300 m (Fig. 2Bb) in the northern and central third, respectively, this whole area most probably experienced periglacial conditions during Quaternary cold periods. By contrast, the VM's southern third (with mean elevations >700 m) exhibit glacially overprinted landscapes. Numerous well-developed cirques along the main topographic divide, U-shaped valleys, glacial deposits (e.g. moraines; Fig. 2Bc), along with glacial and fluvio-glacial deposits blanketing the valley floors (Supplementary Material, Fig. A1) all indicate large-scale, past glacial activity. Despite the lack of numerical dating on glacial landforms, these landscapes bear witness of several Quaternary glaciations characterised by various ice extents (Fig. 1E). Flageollet (2002) recognised at least three to five glaciations. Spatial extensions of the supposedly Last Glacial Maximum (Marine Isotope Stage – MIS2) and the penultimate glaciation (MIS6) are judged reliable because they are based on abundant field evidence, contrasting with the poorly constrained pre-MIS6 glaciations (Supplementary Material, Fig. A2). However, the study of sedimentary formations located at the VM's south(west-)ern margin lead Ménillet (2019) to consider the occurrence of Vosgian glaciations during the Early Pleistocene whose remains were erased during subsequent cold episodes. We thus suggest that the VM has repeatedly experienced significant glaciations over the whole Quaternary.

3. Data and methodology

3.1. Lithology, morphometry and climate

Massif-scale lithology was characterised using the 1:50.000 vectorised geological map provided by the French Geological Survey (BRGM; https://infoterre.brgm.fr/formulaire/telechargement-cartes-geologiques-departementales-150-000-bd-charm-50, last access 29th January 2021). We performed a query-attribute reclassification to obtain five main lithologies for bedrock units: plutonic, metamorphic, volcanic and two classes in sedimentary rocks, i.e. sandstone (mostly Triassic sandstones) and marno-calcareous (at the VM's margins). Quaternary deposits were treated separately and likewise subdivided into alluvial, colluvial and glacial/fluvio-glacial sediments. The respective proportions of each rock and deposit class were extracted within each sampled catchment (Fig. 3). Hierarchical clustering analysis was applied to our dataset of 21 catchments based on the aforementioned lithological classes. Further details on the method is given in Supplementary Material (part 1.1). We used the 25 m-resolution digital elevation model (DEM) provided by the French National Institute of Geography (BD ALTI) to compute three commonly used catchment-averaged metrics: elevation, slope and channel steepness index. For each DEM pixel, slope was computed as the steepest gradient between the eight neighbouring pixels, using the function *terrain* of the *raster* package in R (Hijmans, 2022). Normalised channel steepness index (k_{sn}) was computed using the LSD Topotools software (Mudd et al., 2018) with a reference concavity of 0.45 for inter-catchment comparison (Fig. 1C). We finally computed the mean annual precipitation over the VM (8-km resolution; Fig. 1D) from monthly-cumulated precipitation over the 1958-2009 period extracted from the national hydroclimatic database of Météo-France (Vidal et al., 2010). Catchment-averaged values for each topographic and climatic metric (i.e. elevation, slope, channel steepness, precipitation) were finally computed within each studied catchment (Supplementary Material Table S1).

3.2. Sampling strategy, AMS measurements and denudation rates

We sampled 22 stream sediments from 21 distinct rivers (two samples for the Fecht River; Table 1). Our sampling strategy covers all main rivers draining the VM along with some of their intra-massif tributaries (Fig. 1). Individual catchment sizes range from 62 to 1037 km² and the total surface considered in this study represents ~4,650 km² (Fig. 1). Sampling sites were selected at the outlet of the rivers' mountainous reach. Buechi et al.'s (2014) sampling strategy, primarily focusing on fluvially overprinted landscapes over glacially overprinted landscapes, was adapted with slight modifications (Figs. 1E, 2): the northern and southern parts of the sampled catchments overall match the fluvial landscapes and the glacial and fluvio-glacial landscapes, respectively.

River-sand samples were dried and sieved at the 250-1000 µm grain-size fraction. All ^{26}Al and ^{10}Be chemical extractions and were performed at LN2C (National Laboratory of Cosmogenic Nuclides) located at the Centre Européen de Recherche et d'Enseignement des Géosciences de l'Environnement (CEREGE) laboratory in Aix-en-Provence (France) following standard procedures (e.g. Braucher et al., 2011; see Supplementary Material part 1.2 for further details). AMS measurements took place at the French national Facility, ASTER (Arnold et al., 2010). Measurement calibrations of the beryllium and aluminium measurements were done using the STD-11 standard (^{10}Be/^{9}Be ratio of 1.191 x 10^{-11} ±1.08%; Braucher et al., 2015) and the ASTER in-house standard SM-AL-11 (^{26}Al/^{27}Al ratio of 7.401 ±0.064 x 10^{-12}; Merchel & Bremser, 2004), respectively. The reported analytical uncertainties (1σ) include both the AMS counting statistics and internal error (0.5% for ^{10}Be; Arnold et al., 2010), chemical blank measurement and ^{27}Al measurements. ^{10}Be/^{9}Be blank ratio was 2.15 x 10^{-15} and ^{26}Al/^{27}Al blank ratio was less than 7.02 x 10^{-16}.

CWD rates were inferred from ^{10}Be and ^{26}Al concentrations using the software CosmoCalc version 3.1 (https://www.ucl.ac.uk/~ucfbpve/cosmocalc/; Vermeesch, 2007), based on the time-independent Lal (1991)/Stone (2000) scaling model. The 22 catchments were first delineated using the 25-m resolution DEM and standard hydrological routing procedures. Latitude of each catchment's centroid as well as their average elevation were then calculated. For the sea-level-high-latitude (SLHL) reference production rates of ^{10}Be and ^{26}Al, we used the default values implemented in CosmoCalc version 3.1 which are 4.3 and 30.95 at/g/a, respectively. Muonic productions was based on the scheme of Braucher et al. (2011). We assumed a standard bedrock density of 2.7 g/cm³ and did not apply any production correction for topographic shielding as reported by DiBiase (2018), nor for snow shielding.

4. Results

4.1. Lithological, morphometric and climatic spatial patterns

The spatial distribution of the different bedrock lithologies and Quaternary deposits reveals significant spatial variations over the VM and the 22 sampled catchments (Fig. 3). Some catchments are clearly dominated by a single main lithology, such as plutonic (e.g. #13, 20) and metamorphic (e.g. #7) bedrocks or sandstone (e.g. #10, 15). By contrast, other catchments are either constituted of two (e.g. #5, 14) or more (e.g. #1, 19) dominant lithologies. The hierarchical clustering analysis results in four catchments classes that are named after their main respective lithological composition: metamorphic (m), plutonic (p), sedimentary (s) and volcanic (v). The relative proportions of Quaternary deposits in each catchment not only significantly vary, ranging from 4.5% (#6) to 48.3% (#2), but the prevailing type of Quaternary deposits also differs with dominant alluvial, colluvial and glacial/fluvio-glacial sediments in e.g. catchments #16, 11 and 14, respectively (Fig. 3). Further details on the lithological specificities of each group of catchments are given in Supplementary Material (part 2.1).

Latitudinal variations in catchment-averaged elevation, slope, k_{sn} and annual precipitation range from 260 to 862 m, 8 to 21°, 8 to 69 $m^{0.9}$ and 748 to 1767 mm, respectively (Table 1 and Fig. 4). Whereas elevation, slope and annual precipitation vary by a factor of 2 to 3 at the massif scale, a southward increasing trend in k_{sn} of almost one order of magnitude is documented. Mean elevation (Fig. 4A), slope (Fig. 4B), k_{sn} (Fig. 4C) and annual precipitation (Fig. 4D) all display a significant inverse correlation with the catchment-centroid latitude (R^2=0.42-0.81) and thereby attest the VM's N-S gradient. A secondary W-E gradient is also observed for topographic and climatic metrics, with two diverging trends. Unlike slope and k_{sn} values that are higher in the east than in the west (Fig. 4B-C), higher annual precipitation are recorded in the west (Fig. 4D). No significant W-E difference is found concerning the elevation (Fig. 4A).

4.2. ^{10}Be and ^{26}Al concentrations and ^{26}Al/^{10}Be ratios

Measured ^{10}Be and ^{26}Al concentrations, calculated ^{26}Al/^{10}Be ratios and associated uncertainties are presented in Table 1. ^{10}Be and ^{26}Al concentrations range from 6.1(±0.2) to 13.7(±0.5) x 10^4 at/g and from 11.1(±2) to 92.5(±9) x 10^4 at/g, respectively. ^{26}Al/^{10}Be ratios for the 22 samples range from 1.4 ±0.2 to 8.0 ±0.7. ^{26}Al/^{10}Be ratios are plotted in the two-nuclide diagram (Lal, 1991; Fig. 5A) using CosmoCalc version 3.1 (Vermeesch, 2007) with the time-independent Lal (1991)/Stone (2000) scaling model. In this diagram, the steady-erosion island is comprised between two lines representing the evolution of the ^{26}Al/^{10}Be ratio in material being continuously exposed without erosion (upper line) and varying steady erosion rates (lower line). Thirteen samples (#1, 4, 5, 7, 8, 9, 10, 11, 15, 16, 17, 20, 21) out of 22 modern stream samples (~60%) plot within the steady-erosion island, considering 2σ uncertainties (Fig. 5A). They are referred to as the *steady-state samples* hereinafter. The remaining nine samples (#2, 3, 6, 12, 13, 14, 18, 19, 22) plot below the steady-erosion island, considering 2σ uncertainties (Fig. 5A). In the so-called complex exposure zone, these samples show different apparent burial durations (i.e. minimum burial times) due to their varying depleted ^{26}Al/^{10}Be ratios (Fig. 5A): these range from ~500 ka (#6, 22) to more than 3 Ma (#2, 14; Table 1). They are referred to as the *non-steady-state samples* hereinafter.

4.3. Catchment-averaged denudation rates

We consider here the whole dataset regardless of the individual ^{26}Al/^{10}Be ratios (Table 1 and Fig. 5B). CWD rates and integration times inferred from ^{10}Be concentrations range from 34±1 to 88±4 mm/ka (catchments #11; 3) and 6.8 to 17.6 ka, respectively. Those inferred from ^{26}Al concentrations range from 41±3 to 363±53 mm/ka (catchments #11; 2) and 1.7 to 14.5 ka, respectively (Table 1 and Fig. 5B). First, when comparing ^{10}Be and ^{26}Al-inferred CWD rates (Fig. 5B), the *steady-state samples* are well distributed along the 1:1 line (± 25%). By contrast, among the nine *non-steady-state samples*, seven of them (#2, 3, 12, 13, 14, 18, 19) clearly plot apart from the 1:1 line (Fig. 5B). Almost all ^{26}Al-inferred CWD rates are significantly higher than ^{10}Be-inferred values, sometimes by a factor four or higher (#2 and 14). Second, we plot the latitude of the catchments' centroid against CWD rates inferred from both nuclides, alongside the four lithological groups and the mean annual precipitation (Fig. 6). On the eastern side, a southward increasing trend is highlighted for both ^{10}Be and ^{26}Al-derived CWD rates. On the western side, no clear spatial pattern can be observed, neither for ^{10}Be nor for ^{26}Al. Importantly, the seven *non-steady-state* samples showing the largest discrepancies in ^{10}Be- versus ^{26}Al-CWD rates are all located in the southern part of the VM (Fig. 6), regardless the catchment lithology and annual precipitation.

5. Discussion

5.1. What can - and cannot - be said about spatial denudation patterns in the Vosges Mountains?

5.1.1. Unsteadiness blurs cosmogenic nuclide signals at the massif scale

A global southward increasing trend in elevation, slope, k_{sn} and annual precipitation is highlighted throughout the VM together with a clear latitudinal distribution of the main bedrock lithologies (Figs. 3, 4). These have been proposed as the primary factors governing catchment-wide denudation based on ^{10}Be measured in active stream sediments (e.g. Safran et al., 2005; Carretier et al., 2013; Cyr et al., 2014; Mandal et al., 2015; Olen et al., 2016; Olivetti et al., 2016; Delunel et al., 2020; Peifer et al., 2021). Correlations are thus tested for elevation, slope, k_{sn} and annual precipitation (Fig. 7; Table A in Supplementary Material). Only one significant relationship (though weak: R^2=0.22-0.24; p-value<0.03) is observed between annual precipitation and CWD rates inferred from both nuclides and based on the whole VM dataset (Fig. 7B, E).

One must recall, however, that nine catchments (#2, 3, 6, 12, 13, 14, 18, 19, 22; ~40%) violate the steady-state assumption required to infer denudation rates from measurement of *in situ* cosmogenic nuclides concentrations in river sediments (von Blanckenburg, 2005; Dunai, 2010). Accordingly, these *non-steady-state samples* should be discarded when it comes to (i) infer CWD rates at the massif scale and (ii) correlate these with potential controlling factors (climatic and/or morphometric control). Discarding these catchments has a strong impact as they represent a total drainage area of ~1,987 km² (i.e. 43% of the study area; Fig. 1). Moreover, these catchments are mostly located in the VM's southern part (7/9) and thereby substantially reduce the relationship between the VM's N-S structuration and the spatial pattern of denudation (Fig. 7). Unsteadiness in cosmogenic nuclide concentrations measured in modern river sediments from nine catchments thus prevents any conclusions regarding the controlling factors at the whole massif scale.

Two subsets can be distinguished among *non-steady-state samples*: the northern ones (# 6 and 22) have slightly depleted ^{26}Al/^{10}Be ratios (5.7±0.5) whereas the southern ones (#2, 3, 12, 13, 14, 18, 19) have much lower ratios (1.4±0.2–5.2±0.6; Fig. 5A; Fig. 6). Whilst ^{10}Be- and ^{26}Al-inferred CWD rates of the first group overlap the 25% uncertainty space around the 1:1 line defined by both nuclides (Fig. 5B), those of the second group systematically plot apart from it. We assume that the first two samples (# 6 and 22) might possibly fall into the range of uncertainties related to methodological effects on depletion of ^{26}Al/^{10}Be production ratios (Wittmann et al., 2020). On the other hand, the strongly depleted ^{26}Al/^{10}Be ratios peculiar to the second group cannot be explained by intrinsic uncertainties linked to the production ratio or attenuation lengths. One must consider instead the effect(s) of one or several geomorphological processes since no significant relationship is observed between catchment area and ^{26}Al/^{10}Be ratios at the massif scale (Supplementary Material, Table A, Fig. C).

5.1.2. Lithological and vegetation potential control on denudation for steady-state catchments

With removing the nine *non-steady-state* samples, the range of ^{10}Be- and ^{26}Al-derived CWD rates in the thirteen steady-state catchments is significantly reduced to 34±1 – 66±2 and 41±3 – 73±7 mm/ka, respectively. ^{10}Be-derived CWD from a small unglaciated catchment located between our catchments #8 and 20 fall in the same range (i.e. ~38 mm/ka; Ackerer et al., 2022). By contrast, in these thirteen catchments, the observed large ranges in mean elevation, k_{sn} and annual precipitation remains as in the initial dataset (see 4.1) and only the slope fractionally decreases (between 8.3 and 20.4°; Table 1). Yet, none of the above morphometric and climatic controlling factors appears playing a major role here, as shown by the absence of significant correlation with CWD rates inferred from both nuclides (Supplementary Material Table A; Fig. B).

The VM denudation pattern, including the previously-reported lack of correlation with morphometric/climatic parameters, can be tentatively explained by two main features peculiar to this low-elevation mid-latitude mountain range. First, deciduous, resinous and mixed forests currently cover ~70% of its surface (Rochel, 2004), mostly on hillslopes and interfluve areas (Fig. 2B). They were probably even more widespread before the Middle Age as forest clearance linked to past agricultural practices occurred at that time (Keller et al., 2023). Whilst vegetation has been increasingly considered as a controlling or modulating factor on CWD rates (e.g. Mandal et al., 2015; Olen et al., 2016; Schaller et al., 2018), Acosta et al. (2015) reported lower denudation rates in areas covered by dense vegetation. We likewise suggest that, in addition to this possible denudation lowering effect from dense vegetation, the VM's dense forest cover could have smoothed the variability in topographic surface erodibility. This would have resulted in lower amplitude of CWD rates that do not much differ across the thirteen investigated catchments, despite the contrasted ranges in elevation, slope, k_{sn} and annual precipitation.

Second, and more importantly, the lithological heterogeneity encountered within the thirteen *steady-state* catchments possibly overprints the other controlling factors (Morel et al., 2003; Campforts et al., 2020). In the following we compare the crystalline- (#4, 5, 7, 8 and 20) and sedimentary-dominated (# 1, 9, 10, 15, 16 and 21) catchments (Figs. 3 and 6). Although mean k_{sn} value of the crystalline group (~58 $m^{0.9}$) is about three times higher than that of the sedimentary group (~19 $m^{0.9}$), ^{10}Be- and ^{26}Al-derived CWD do not significantly differ between both groups: ~53/~60 mm/ka versus ~51/~52 mm/ka in crystalline and sedimentary catchments, respectively (Supplementary Material, Fig. B). Despite an observed lower magnitude in relief incision (i.e. ~150 m) in the sedimentary-dominated landscapes of the northern VM, denudation there is assumed to be as high as in the much more incised southern part (Figs. 1C and 2). The observed similarity in CWD rates obtained for both lithological groups thus implies that the erodibility of the homogeneous cover of Triassic sandstones should be much higher than that of Palaeozoic granites and gneisses. Note that all these catchments are located at the margins of the former glacier extents and, accordingly, must have experienced periglacial conditions during Quaternary cold stages. In addition, sandstone's enhanced erodibility due to periglacial processes has been already recognised in Palaeozoic, European low-mountain ranges (e.g. Ardennes in Belgium, Rixhon and Juvigné, 2010) and was recently quantified by cosmogenic nuclides in sandstone-dominated catchments for the central Appalachians (Del Vecchio et al., 2022).

5.2. Understanding the impacts of former glaciations on cosmogenic nuclide disequilibrium

One of the main outcomes of this study is the spatial correlation between catchments in cosmogenic disequilibrium and the reconstructed former glaciations covering the southern VM. Our aim here is to assess the impact of glaciations on the depletion of the ^{26}Al/^{10}Be ratio through two processes, glacial shielding and reworking of previously buried sediment. Among all processes listed by Wittmann et al. (2020) resulting in depleted Al/Be ratio in river sediments, these two are the only ones that are relevant in the VM.

5.2.1 ^{26}Al/^{10}Be ratio's depletion correlates with repeated glacial shielding

Although glacial shielding is one of the best documented processes to cause ^{26}Al/^{10}Be-ratio lowering in bedrock of high-latitude, formerly glaciated regions (e.g. Corbett et al., 2013; Strunk et al., 2017; Andersen et al., 2018; 2020), it was barely considered when assessing CWD rates from modern stream sediments. In the following, we show a quantitative comparison between ^{26}Al/^{10}Be ratios in modern river sediments and former glacial covers in each catchment attributed to the LGM/MIS2 (Fig. 8A) and the penultimate glaciation/MIS6 (Fig. 8B) because their reconstruction is based on reliable and widespread field evidence (Flageollet, 2002).

Main outputs of this comparison are twofold. First, significant correlations (p-values$\leq$0.0001) are observed between ^{26}Al/^{10}Be ratio and the extent of past glacial cover during MIS2 (R^2=0.53) and 6 (R^2=0.62; Fig. 8A-B). All unglaciated catchments (i.e. <10% of ice cover during MIS2) cluster on the 6.7 production-ratio line, regardless the considered glacial period. The eleven formerly ice-covered catchments show an inverse general trend for both cold periods: the larger the former glacial cover in each catchment, the lower the ^{26}Al/^{10}Be ratio measured in its stream sediments (Fig. 8A-B). This observation underlines the probable link between long-lasting (i.e. 10^{3-4} years) and repetitive ice shielding and unsteadiness in the stream cosmogenic nuclide signal. One must bear in mind here that pre-MIS6 glaciations were documented in the VM's southern part (Flageollet, 2002; Supplementary Material, Fig. A2) and suggested at its southern margin (Ménillet, 2019). We thus propose that shielding in this area probably occurred during many cold periods of the Quaternary even if the correlated deposits of these pre-MIS6 glaciations can only be found in fluvial terrace sequences (e.g. Moselle and Ognon) located at the massif's outskirt (Harmand, 2020). Second, the significance of these relationships increases with larger ice shielding between the two glacial periods: the ice-covered area roughly doubles between MIS2 (~730 km²) and 6 (~1570 km²; Fig. 1E). Note that three catchments were fully ice-covered during the LGM (i.e. >95%; Fig. 8B). We suggest here that this R² increase (0.53 to 0.62) is probably linked to distinct ice dynamics reflected in the spatial pattern peculiar to each cold stage (Flageollet, 2002; Fig. 1E). The LGM was characterised by a mosaic of valley glaciers with various ice-flow directions and lengths (up to ~40 km in the Moselle, #12), leaving large parts of the VM's main divide and secondary ridges ice-free (Supplementary Material, Fig. A2). By contrast, only a handful of small-dimensioned nunataks protruded the almost continuous MIS6's ice field characterised by a former SW-NE extent of ~60 km (Supplementary Material, Fig. A2).

Although reconstructing the thermal nature of the former glacial masses in the southern VM is beyond the scope of this study, two lines of arguments based on previous studies using ^{10}Be and ^{26}Al measurements could point to limited subglacial erosion and thus previous cold-based ice cover. First, if occurrence of cold-based glaciers is traditionally assigned to arctic regions (Copland, 2013), the highest ridges in the northern Appalachians, i.e. a similar setting to the southern VM, were covered by cold-based ice during the LGM (Bierman et al., 2015). Second and most important, depleted ^{26}Al/^{10}Be ratios in bedrock and erratics from Greenland were well explained by prolonged and repeated burial beneath cold-based ice during glaciations (Corbett et al., 2013). The same holds for glacial tills shielded by cold-based ice on the Baffin Island, where the sampled grain size matches the sandy fraction studied here (Staiger et al., 2006). The depleted ^{26}Al/^{10}Be ratios of these eight sandy samples (i.e. 1.3 to 4.3) fall into a similar range to ours (1.4 to 5.2). Such depleted values would imply minimum burial times ranging from ~500 ka to ~3 Ma (Fig. 5; Table 1). If this continuous burial duration was indeed observed on Baffin Island, it is not so in the VM, whose relief has certainly been re-exposed to radiation during each interglacial period. It therefore seems highly probable that VM sediments were not correctly re-exposed to cosmic-rays between glaciations. Knudsen and Egholm's (2018) modelling results showed that very low ^{26}Al/^{10}Be ratios may not be exclusively explained by prolonged burial under non-erosive ice, but may also reflect spatio-temporally varying bedrock exposure/burial and erosion histories. In addition to ice shielding, we therefore suggest that repeated, complex sediment routing systems during deglaciation and subsequent interglacial periods probably characterised the formerly glaciated catchments of the VM, thereby explaining the depleted ^{26}Al/^{10}Be ratios measured in the stream sediments.

5.2.2. ^{26}Al/^{10}Be ratio's depletion correlates with the amount of glacial sediment storage

Successive sediment burial and reworking within a sediment routing system, sometimes for long periods of time (i.e. > 10^5 years; Fülöp et al., 2020; Bhattacharjee et al., 2023) or rapid changes in denudation rates may yield to depleted ^{26}Al/^{10}Be ratio measured in the stream sediments. Although the cosmogenic nuclide signal is likely to be preserved from the source area to the sink in most cases (Wittmann et al., 2009), a handful of studies highlighted a significant decrease in ^{26}Al/^{10}Be ratios measured in stream sediments from glaciated catchments (Safran et al., 2005; Hippe et al., 2012; Grin et al., 2018; Wittmann et al., 2020; Zhang et al., 2021). Glacial environments are generally well-known to have complex sediment routing systems (e.g. Porter et al., 2019). Based on CWD rates inferred from both nuclides, Zhang et al. (2021) also identified this issue but did not provide further explanations regarding the correlated processes. This study presents, to our knowledge, the first quantitative comparison between ^{26}Al/^{10}Be ratios in modern river sediments and the surficial proportions of Quaternary deposits at the individual catchment scale (Fig. 8C-D).

When all Quaternary sediments are considered, regardless of their nature, a significant correlation is observed ($R^2=0.33$; p-value<0.01; Fig. 8C). When only glacial/fluvio-glacial sediments are considered, the strongest correlation is observed among all our proxies to assess glacial impact on measured ^{26}Al/^{10}Be ratios ($R^2=0.67$; p-value<0.0001; Fig. 8D), including ice-cover shielding. Whereas all unglaciated catchments cluster on the 6.7 production-ratio line, higher depletions of ^{26}Al/^{10}Be ratios are observed with increasing percentage of glacial sediments, peaking in catchment #2 (Fig. 8D). This suggests that (i) glacially-reworked deposits contain more ^{26}Al/^{10}Be-depleted material than fluvial and colluvial ones, and (ii) the greater the amount of glacial deposits present in the catchment, the greater the likelihood for the current river channel to rework these deposits.

A closer look at the spatial distribution of glacial/fluvio-glacial deposits throughout the southern VM clearly highlights a W-E gradient, with the highest proportions of glacial/fluvio-glacial sediments encountered in the west-flowing catchments (i.e # 2, 12, 13, 14, 17, 19; Fig. 8D and Supplementary Material Fig. A1). One must recall here the geologically controlled W-E increasing gradient in mean catchment slope: 12.6 vs 16.9° to the west and the east of the main divide, respectively. Efficient sediment transfer in the east-flowing catchments can be assumed because of (i) shorter transport distances (Fig. 1B), (ii) higher mean slopes (Fig. 4B), (iii) much lower proportions of glacial deposits along their intra-massif reaches (Supplementary Material Fig. A1) and (iv) km-large, thick, Quaternary alluvial fans extending at the eastern Vosgian footslopes (e.g. catchments #1, 4, 6, 8, 18; Wuscher, 2021). As a result, only one of the east-flowing catchments (#3) plots apart from the 6.7 line (Fig. 8).

By contrast, among the six west-flowing, formerly glaciated catchments, five of them show depleted ^{26}Al/^{10}Be ratios (Fig. 8). This probably reveals more complex sediment routing systems and the catchment #2 (i.e. the so-called Cleurie) with the most depleted ratio of our whole dataset (~1.4) epitomises this. First, if this catchment belongs to the group of catchments that were significantly and repeatedly covered by glaciers (#2, 12, 13, 14; Fig. 8A-B), it clearly stands out because of the highest relative proportion of glacial/fluvio-glacial sediments (i.e. >40% vs ≤20% for the rest; Fig. 8D). Though being the second smallest catchment investigated in this study (<80 km²; Table 1), the Cleurie accordingly hosts the highest density and largest diversity of glacial and glacial-related landforms, including e.g. end-moraines, kame terraces, lacustrine and deltaic deposits (Seret, 1967; Flageollet, 2002). Second, thicknesses of valley-floor sediments exceeding 50 m, though undated, were revealed by drillings performed in the uppermost part of the catchment (BRGM). Third, petrographical and mineralogical analyses performed in some of these deposits reveal a partially allochthonous origin for some of the sampled materials, i.e. from the catchment located to the south (#13; Flageollet, 1971). Fourth, the peculiar spatial distribution and geometry of the best-preserved, i.e. tens of meters high, end moraines strongly point to a triple convergence of valley glaciers supposedly occurring during the LGM and peaking in the formation of a palaeolake in the catchment's upstream part (Flageollet, 2002). Fifth, a major flood occurred in the valley in 1770, whose damages were mapped in an archive document (Salmon, 1770). The latter reveals erosion and reworking of glacial material buried at the base of the highest moraines. Altogether, the concentration and diversity of glacial(-related) landforms along with the long-lasting storage of reworked and partially allochthonous material (i.e. "stop-and-go", possibly similar to foreland glacial systems, e.g. Cogez et al., 2018) suggests a very complex sediment routing system in the Cleurie which yields the most depleted $^{26}Al/^{10}Be$ ratio of our dataset. More generally, our findings suggest that the sediments sampled in the SW catchments of the VM could have survived several glacial cycles. They might have been shielded by cold-based ice during glaciations, without being sufficiently re-exposed to cosmic rays during interglacial periods as they were buried underneath thick glacial sediments. Measuring low $^{26}Al/^{10}Be$ ratios in modern stream sediment also implies that the river network is currently partly supplied by depleted $^{26}Al/^{10}Be$ sedimentary material.

5.3. *Regional denudation in the Vosges and Black Forest Mountains*

At the regional scale, we compare our CWD rates with those previously obtained in SW Germany in the neighbouring Black Forest Mountains which shows a similar overall N-S structuration in lithology, elevation and morphometry. We recalculated fifty ^{10}Be-inferred CWD rates published by Morel et al. (2003), Meyer et al. (2010) and Glotzbach et al. (2013) using the methodology reported above to allow quantitative comparisons (see Supplementary Material, part 1.3). All sampled catchments are located within a similar latitude range than the VM (Fig. 9); they can thus be compared in terms of lithology, elevation and morphometry. The median (and standard deviation) ^{10}Be-derived CWD rates for the Black Forest Mountains and VM, regardless of the cosmogenic nuclide steadiness of the samples, appear at first glance remarkably similar: 52.6±23.6 and 52.9±14.4 mm/ka, respectively (Fig. 9). However, two complications considerably hamper a meaningful comparison between the two datasets. First, the average drainage area of the Black Forest Mountains catchments (~27 km²) is one order of magnitude smaller than for the VM catchments (~262 km²; Fig. 9A). Moreover, a majority of these small catchments are located in the headwaters of three main rivers draining the Black Forest Mountains, i.e. the Danube, Kinzig and Wutach. This strongly contrasts with our sampling strategy consisting in sampling all main rivers draining the VM. Second and most importantly, almost all catchments sampled by Morel et al. (2003) and Glotzbach et al. (2013) are located within the former MIS6 glacier extent (specific sampling approach to investigate the impact of glacial erosion and ice cover on CWD rates). However, the sole ^{10}Be measurement in modern stream sediments in these studies leave this twofold fundamental question open: considering a cosmogenic nuclide non-steady state (Glotzbach et al., 2013), how much disequilibrium characterises the sampled material there?

6. Conclusions and perspectives

From the massif-scale characterisation coupled to the paired-nuclide analysis to infer ^{10}Be- and ^{26}Al-based catchment-wide denudation rates across the Vosges Massif, we can conclude that:

(i) elevation, slope, k_{sn} and precipitation are primarily organised along a N-S increasing trend while a subordinated E-W gradient occurs;

(ii) ^{10}Be- and ^{26}Al-derived catchment-wide denudation rates range from 34±1 to 66±2, and 41±3 to 73±7 mm/ka, respectively, in thirteen steady-state catchments that are in cosmogenic equilibrium;

(iii) nine samples have depleted ^{26}Al/^{10}Be ratios (up to 1.4) and they mostly cluster in the Vosges Massif's area (SW) which was the most intensively glaciated during Quaternary cold stages. They reveal cosmogenic nuclide unsteadiness in modern river sediments and must be accordingly discarded when it comes to infer catchment-wide denudation rates, thereby precluding any conclusion about controlling factors at the whole massif scale;

(iv) no relationship is reported between elevation, slope, k_{sn} and precipitation, and catchment-wide denudation rates in the steady-state catchments. Instead, lithological contrasts may control the pattern of denudation with a higher erodibility, especially under periglacial conditions, of the sandstone-dominated catchment compared to the crystalline-dominated catchments. We also suggest that the dense and almost ubiquitous vegetation cover reduces the variability in erodibility;

(v) a statistically significant relationship is observed between the degree of depletion of the ^{26}Al/^{10}Be ratios and the spatial pattern of glaciation: the larger the former glacial cover in each catchment, the lower the ^{26}Al/^{10}Be ratio measured in its stream sediments. It underlines the link between long-lasting and repetitive ice shielding and unsteadiness in the stream cosmogenic signal. It also possibly suggests the past existence of cold-based glaciers in the Vosges Massif.

(vi) an even more significant relationship is reported between the degree of depletion of the ^{26}Al/^{10}Be ratios and the increasing proportion of glacial and fluvio-glacial deposits within each catchment. It underlines the link between complex sediment routing systems in glacial environments and unsteadiness in the stream cosmogenic signal. This also well aligns with an E-W gradient: efficient sediment transfer versus longer sediment storage in the east- and west-flowing catchments, respectively. The catchment with the lowest ^{26}Al/^{10}Be ratio (1.4) remarkably matches the most complex sediment routing system from all sampled catchments.

This study raises several key points. First, we argue for systematic measurements of ^{26}Al to complement ^{10}Be and to test the steady-state assumption when it comes to infer catchment-wide denudation rates from modern stream sediments, especially in formerly glaciated landscapes. Second, we show that 86% of the catchments containing more than 10% of glacial/fluvio-glacial deposits (6/7) have depleted ^{26}Al/^{10}Be ratio and are thus in cosmogenic nuclide disequilibrium. A good knowledge of the regional glacial history, including quantitative and chronological data, is thus prerequisite and this 10% occurrence of glacial/fluvio-glacial deposits could be used, at first glance, as a threshold value. Third, despite strong quantitative evidence of ^{26}Al/^{10}Be ratio depletion trough glacial related processes, further work is required to improve our interpretations. As for the impact of former ice covers, one should refine their spatial extents, assess their palaeothicknesses and chronologies. Abundant erratics and moraine deposits are key landforms here. ^{10}Be and ^{26}Al measurements of glacially polished bedrock should also be performed to assess glacial erosion efficiency and test the assumption of former cold-based glaciers. As for the impact of complex sediment-routing system, along stream ^{10}Be and ^{26}Al measurements should be undertaken in both east- and west flowing catchments. Dating valley-floor sediments and sediment budgeting of Vosgian valleys would bring key elements as well.

CRediT authorship contribution statement

Timothée Jautzy: Conceptualisation, Methodology, Investigation, Visualisation, Software, Writing – Original draft. **Gilles Rixhon:** Funding acquisition, Conceptualisation, Methodology, Investigation, Visualisation, Writing – Original draft. **Régis Braucher:** Conceptualisation, Methodology, Investigation, Writing – Review & Editing. **Romain Delunel:** Conceptualisation, Methodology, Writing – Review & Editing. **Pierre G. Valla:** Conceptualisation, Methodology, Writing – Review & Editing. **Laurent Schmitt:** Funding acquisition. **ASTER Team:** Formal analysis – AMS measurements.

Acknowledgements

Support for this research was provided by the University of Strasbourg (IDEX, France), the Scientific Council of the National School for Water and Environmental Engineering of Strasbourg (ENGEES, France), the Grand Est region (France), the Rhine-Meuse Water Agency (AERM, France) and the River Union Haute Alsace (France). P.G.V. acknowledges funding from the French ANR-PIA program (ANR-18-MPGA-0006). The ASTER AMS national facility (CEREGE, Aix en Provence) is supported by the INSU/CNRS, the ANR through the "Projets thématiques d'excellence" program for the "Equipements d'excellence" ASTER-CEREGE action and IRD. This manuscript benefited from constructive reviews from B. Bookhagen and an anonymous reviewer from Potsdam who are thanked for their insightful comments and suggestions.

References

Ackerer, J., Van der Woerd, J., Meriaux, A. S., Ranchoux, C., Schäfer, G., Delay, F., & Chabaux, F. (2022). Quantifying geomorphological evolution from 10Be denudation rates: Insights from high-resolution depth profiles, topsoils, and stream sediments (Strengbach CZO, France). Earth Surface Processes and Landforms, 47(14), 3239–3258. https://doi.org/10.1002/esp.5454

Acosta, V. T., Schildgen, T. F., Clarke, B. A., Scherler, D., Bookhagen, B., Wittmann, H., von Blanckenburg, F., & Strecker, M. R. (2015). Effect of vegetation cover on millennial-scale landscape denudation rates in East Africa. Lithosphere, 7(4), 408–420. https://doi.org/10.1130/L402.1

Andersen, J. L., Egholm, D. L., Knudsen, M. F., Linge, H., Jansen, J. D., Pedersen, V. K., Nielsen, S. B., Tikhomirov, D., Olsen, J., Fabel, D., & Xu, S. (2018). Widespread erosion on high plateaus during recent glaciations in Scandinavia. Nature Communications, 9(1), 830. https://doi.org/10.1038/s41467-018-03280-2

Andersen, J. L., Egholm, D. L., Olsen, J., Larsen, N. K., & Knudsen, M. F. (2020). Topographical evolution and glaciation history of South Greenland constrained by paired 26Al/10Be nuclides. Earth and Planetary Science Letters, 542, 116300. https://doi.org/10.1016/j.epsl.2020.116300

Arnold, M., Merchel, S., Bourlès, D. L., Braucher, R., Benedetti, L., Finkel, R. C., Aumaître, G., Gottdang, A., & Klein, M. (2010). The French accelerator mass spectrometry facility ASTER: Improved performance and developments. Nuclear Instruments and Methods in Physics Research Section B: Beam Interactions with Materials and Atoms, 268(11–12), 1954–1959. https://doi.org/10.1016/j.nimb.2010.02.107

Bhattacharjee, S., Bookhagen, B., Sinha, R., Wieser, A., & Marchhart, O. (2023). 26Al and 10Be concentrations from alluvial drill cores across the Indo-Gangetic plain reveal multimillion-year sediment-transport lag times. Earth and Planetary Science Letters, 619, 118318. https://doi.org/10.1016/j.epsl.2023.118318

Bierman, P. R., Davis, P. T., Corbett, L. B., Lifton, N. A., & Finkel, R. C. (2015). Cold-based Laurentide ice covered New England's highest summits during the Last Glacial Maximum. Geology, G37225.1. https://doi.org/10.1130/G37225.1

Braucher, R., Guillou, V., Bourlès, D. L., Arnold, M., Aumaître, G., Keddadouche, K., & Nottoli, E. (2015). Preparation of ASTER in-house 10Be/9Be standard solutions. Nuclear Instruments and Methods in Physics Research Section B: Beam Interactions with Materials and Atoms, 361, 335–340. https://doi.org/10.1016/j.nimb.2015.06.012

Braucher, R., Merchel, S., Borgomano, J., & Bourlès, D. L. (2011). Production of cosmogenic radionuclides at great depth: A multi element approach. Earth and Planetary Science Letters, 309(1–2), 1–9. https://doi.org/10.1016/j.epsl.2011.06.036

Buechi, M. W., Kober, F., Ivy-Ochs, S., Salcher, B., Kubik, P. W., & Christl, M. (2014). Denudation rates of small transient catchments controlled by former glaciation: The Hörnli nunatak in the northeastern Swiss Alpine Foreland. Quaternary Geochronology, 19, 135–147. https://doi.org/10.1016/j.quageo.2013.06.005

Campforts, B., Vanacker, V., Herman, F., Vanmaercke, M., Schwanghart, W., Tenorio, G. E., Willems, P., & Govers, G. (2020). Parameterization of river incision models requires accounting for environmental heterogeneity: Insights from the tropical Andes. Earth Surface Dynamics, 8, 447–470.

Carretier, S., Regard, V., Vassallo, R., Aguilar, G., Martinod, J., Riquelme, R., Pepin, E., Charrier, R., Hérail, G., Farías, M., Guyot, J.-L., Vargas, G., & Lagane, C. (2013). Slope and climate variability control of erosion in the Andes of central Chile. Geology, 41(2), 195–198. https://doi.org/10.1130/G33735.1

Cogez, A., Herman, F., Pelt, É., Reuschlé, T., Morvan, G., Darvill, C. M., Norton, K. P., Christl, M., Märki, L., & Chabaux, F. (2018). U–Th and 10Be constraints on sediment recycling in proglacial settings, Lago Buenos Aires, Patagonia. Earth Surface Dynamics, 6(1), 121–140. https://doi.org/10.5194/esurf-6-121-2018

Copland, L. (2013). Classification of Ice Masses. In J. Shroder, R. Giardino, & J. Harbor (Eds.), Treatise on Geomorphology (Academic Press, Vol. 8, pp. 45–52). Elsevier.

Corbett, L. B., Bierman, P. R., Graly, J. A., Neumann, T. A., & Rood, D. H. (2013). Constraining landscape history and glacial erosivity using paired cosmogenic nuclides in Upernavik, northwest Greenland. Geological Society of America Bulletin, 125(9–10), 1539–1553. https://doi.org/10.1130/B30813.1

Cyr, A. J., Granger, D. E., Olivetti, V., & Molin, P. (2014). Distinguishing between tectonic and lithologic controls on bedrock channel longitudinal profiles using cosmogenic 10Be erosion rates and channel steepness index. Geomorphology, 209, 27–38. https://doi.org/10.1016/j.geomorph.2013.12.010

Darmois-Théobald, M. (1972). Cirques glaciaires et niches de nivation sur le versant lorrain des Vosges à l'Ouest du Donon. Revue Géographique de l'Est, 12(1), 55–67. https://doi.org/10.3406/rgest.1972.1222

Del Vecchio, J., DiBiase, R. A., Corbett, L. B., Bierman, P. R., Caffee, M. W., & Ivory, S. J. (2022). Increased Erosion Rates Following the Onset of Pleistocene Periglaciation at Bear Meadows, Pennsylvania, USA. Geophysical Research Letters, 49(4). https://doi.org/10.1029/2021GL096739

Delunel, R., Schlunegger, F., Valla, P. G., Dixon, J., Glotzbach, C., Hippe, K., Kober, F., Molliex, S., Norton, K. P., Salcher, B., Wittmann, H., Akçar, N., & Christl, M. (2020). Late-Pleistocene catchment-wide denudation patterns across the European Alps. Earth-Science Reviews, 211, 103407. https://doi.org/10.1016/j.earscirev.2020.103407

Delunel, R., Van Der Beek, P. A., Bourlès, D. L., Carcaillet, J., & Schlunegger, F. (2014). Transient sediment supply in a high-altitude Alpine environment evidenced through a 10Be budget of the Etages catchment (French Western Alps). Earth Surface Processes and Landforms, 39(7), 890–899. https://doi.org/10.1002/esp.3494

DiBiase, R. A. (2018). Short communication: Increasing vertical attenuation length of cosmogenic nuclide production on steep slopes negates topographic shielding corrections for catchment erosion rates. Earth Surface Dynamics, 6(4), 923–931. https://doi.org/10.5194/esurf-6-923-2018

Dunai, T. (2010). Cosmogenic Nuclides: Principles, Concepts and Applications in the Earth Surface Sciences. Cambridge University Press.

Flageollet, J.-C. (2002). Sur les traces des glaciers vosgiens. CNRS éditions Paris.

Flageollet, J.-C., Hameurt, J., & Voirin, G. (1971). Les accumulations glaciaires de la vallée de la Cleurie (Vosges). Revue Géographique de l'Est, 11(2), 119–181. https://doi.org/10.3406/rgest.1971.1194

François, D., & Humbert, J. (2000). Quantification spatiale des précipitations. Applications au Nord-Est de la France. Revue Géographique de l'Est, 40(1–2). https://doi.org/10.4000/rge.4159

Fülöp, R.-H., Codilean, A. T., Wilcken, K. M., Cohen, T. J., Fink, D., Smith, A. M., Yang, B., Levchenko, V. A., Wacker, L., Marx, S. K., Stromsoe, N., Fujioka, T., & Dunai, T. J. (2020). Million-year lag times in a post-orogenic sediment conveyor. Science Advances, 6(25), eaaz8845. https://doi.org/10.1126/sciadv.aaz8845

Glotzbach, C., Röttjer, M., Hampel, A., Hetzel, R., & Kubik, P. W. (2013). Quantifying the impact of former glaciation on catchment-wide denudation rates derived from cosmogenic 10Be. Terra Nova, 26(3), 186–194. https://doi.org/10.1111/ter.12085

Godard, V., Burbank, D. W., Bourlès, D. L., Bookhagen, B., Braucher, R., & Fisher, G. B. (2012). Impact of glacial erosion on 10Be concentrations in fluvial sediments of the Marsyandi catchment, central Nepal. Journal of Geophysical Research: Earth Surface, 117(F3), 2011JF002230. https://doi.org/10.1029/2011JF002230

Granger, D. E., & Schaller, M. (2014). Cosmogenic Nuclides and Erosion at the Watershed Scale. Elements, 10(5), 369–373. https://doi.org/10.2113/gselements.10.5.369

Grin, E., Schaller, M., & Ehlers, T. A. (2018). Spatial distribution of cosmogenic 10Be derived denudation rates between the Western Tian Shan and Northern Pamir, Tajikistan. Geomorphology, 321, 1–15. https://doi.org/10.1016/j.geomorph.2018.08.007

Harmand, D. (2020). Le plateau des Mille Etangs: Un fjell de basse altitude. Revue Géographique de l'Est, 60(1–2). https://doi.org/10.4000/rge.9703

Harmand, D., & Cordier, S. (2012). The Pleistocene terrace staircases of the present and past rivers downstream from the Vosges Massif (Meuse and Moselle catchments). Netherlands Journal of Geosciences - Geologie En Mijnbouw, 91(1–2), 91–109. https://doi.org/10.1017/S0016774600001529

Heyman, B. M., Heyman, J., Fickert, T., & Harbor, J. M. (2013). Paleo-climate of the central European uplands during the last glacial maximum based on glacier mass-balance modeling. Quaternary Research, 79(1), 49–54. https://doi.org/10.1016/j.yqres.2012.09.005

Hijmans, R. J. (2022). raster: Geographic Data Analysis and Modeling. https://CRAN.R-project.org/package=raster

Hippe, K., Kober, F., Zeilinger, G., Ivy-Ochs, S., Maden, C., Wacker, L., Kubik, P. W., & Wieler, R. (2012). Quantifying denudation rates and sediment storage on the eastern Altiplano, Bolivia, using cosmogenic 10Be, 26Al, and in situ 14C. Geomorphology, 179, 58–70. https://doi.org/10.1016/j.geomorph.2012.07.031

Keller, B., Herrault, P. A., Schwartz, D., Rixhon, G., & Ertlen, D. (2023). Spatio-temporal dynamics of forest ecosystems revealed by the LiDAR-based characterization of medieval field systems (Vosges Mountains, France). Anthropocene, 42, 100374. https://doi.org/10.1016/j.ancene.2023.100374

Knudsen, M. F., & Egholm, D. L. (2018). Constraining Quaternary ice covers and erosion rates using cosmogenic 26Al/10Be nuclide concentrations. Quaternary Science Reviews, 181, 65–75. https://doi.org/10.1016/j.quascirev.2017.12.012

Lal, D. (1991). Cosmic ray labeling of erosion surfaces: In situ nuclide production rates and erosion models. Earth and Planetary Science Letters, 104(2–4), 424–439. https://doi.org/10.1016/0012-821X(91)90220-C

Mandal, S. K., Lupker, M., Burg, J.-P., Valla, P. G., Haghipour, N., & Christl, M. (2015). Spatial variability of 10Be-derived erosion rates across the southern Peninsular Indian escarpment: A key to landscape evolution across passive margins. Earth and Planetary Science Letters, 425, 154–167. https://doi.org/10.1016/j.epsl.2015.05.050

Ménillet, F. (2019). Les alluvions d’âge miocène à pléistocène moyen sur le seuil de Belfort ; nouvelles observations et hypothèses sur l’évolution de la région durant ces périodes ; âge des dépôts à blocs de grès triasiques de la bordure alsacienne des Vosges. Géologie de La France, 1(2), 18–40.

Merchel, S., & Bremser, W. (2004). First international 26Al interlaboratory comparison – Part I. Nuclear Instruments and Methods in Physics Research Section B: Beam Interactions with Materials and Atoms, 223–224, 393–400. https://doi.org/10.1016/j.nimb.2004.04.076

Mercier, J.-L. (2014). Glacial Imprint on the Main Ridge of the Vosges Mountains. In M. Fort & M.-F. André (Eds.), Landscapes and Landforms of France (pp. 161–169). Springer Netherlands. https://doi.org/10.1007/978-94-007-7022-5_16

Mercier, J.-L., & Jeser, N. (2004). The glacial history of the Vosges Mountains. In Developments in Quaternary Sciences (Vol. 2, pp. 113–118). Elsevier. https://doi.org/10.1016/S1571-0866(04)80061-7

Meyer, H., Hetzel, R., & Strauss, H. (2010). Erosion rates on different timescales derived from cosmogenic 10Be and river loads: Implications for landscape evolution in the Rhenish Massif, Germany. International Journal of Earth Sciences, 99(2), 395–412. https://doi.org/10.1007/s00531-008-0388-y

Morel, P., von Blanckenburg, F., Schaller, M., Kubik, P. W., & Hinderer, M. (2003). Lithology, landscape dissection and glaciation controls on catchment erosion as determined by cosmogenic nuclides in river sediment (the Wutach Gorge, Black Forest). Terra Nova, 15(6), 398–404. https://doi.org/10.1046/j.1365-3121.2003.00519.x

Mudd, S. M., Clubb, F. J., Gailleton, B., & Hurst, M. D. (2018). How concave are river channels? Earth Surface Dynamics, 6(2), 505–523. https://doi.org/10.5194/esurf-6-505-2018

Olen, S. M., Bookhagen, B., & Strecker, M. R. (2016). Role of climate and vegetation density in modulating denudation rates in the Himalaya. Earth and Planetary Science Letters, 445, 57–67. https://doi.org/10.1016/j.epsl.2016.03.047

Olivetti, V., Godard, V., & Bellier, O. (2016). Cenozoic rejuvenation events of Massif Central topography (France): Insights from cosmogenic denudation rates and river profiles. Earth and Planetary Science Letters, 444, 179–191. https://doi.org/10.1016/j.epsl.2016.03.049

Peifer, D., Persano, C., Hurst, M. D., Bishop, P., & Fabel, D. (2021). Growing topography due to contrasting rock types in a tectonically dead landscape. Earth Surface Dynamics, 9(2), 167–181. https://doi.org/10.5194/esurf-9-167-2021

Portenga, E. W., & Bierman, P. R. (2011). Understanding Earth's eroding surface with 10Be. GSA Today, 21(8), 4–10. https://doi.org/10.1130/G111A.1

Porter, P. R., Smart, M. J., & Irvine-Fynn, T. D. L. (2019). Glacial Sediment Stores and Their Reworking. In T. Heckmann & D. Morche (Eds.), Geomorphology of Proglacial Systems: Landform and Sediment Dynamics in Recently Deglaciated Alpine Landscapes (pp. 157–176). Springer International Publishing. https://doi.org/10.1007/978-3-319-94184-4_10

Rixhon, G., & Juvigné, É. (2010). Periglacial deposits and correlated processes in the Ninglinspo valley (Ardenne Massif, Belgium). Geologica Belgica, 13(1–2), 49–60. https://popups.uliege.be/1374-8505/index.php?id=2853

Rochel, X. (2004). Gestion forestière et paysages dans les Vosges d'après les registres de martelages du XVIIIe siècle: Essai de biogéographie historique [PhD Thesis]. Université de Nancy.

Safran, E. B., Bierman, P. R., Aalto, R., Dunne, T., Whipple, K. X., & Caffee, M. (2005). Erosion rates driven by channel network incision in the Bolivian Andes. Earth Surface Processes and Landforms, 30(8), 1007–1024. https://doi.org/10.1002/esp.1259

Salmon. (1770). Carte topographique des dégâts causés par les eaux de l’orage survenu la nuit du vingt-cinq au vingt-six juillet dernier. Archives départementales des Vosges, France; 1C.

Schaller, M., Ehlers, T. A., Lang, K. A. H., Schmid, M., & Fuentes-Espoz, J. P. (2018). Addressing the contribution of climate and vegetation cover on hillslope denudation, Chilean Coastal Cordillera (26°–38°S). Earth and Planetary Science Letters, 489, 111–122. https://doi.org/10.1016/j.epsl.2018.02.026

Seret, G. (1967). Les systèmes glaciaires du bassin de la Moselle et leurs enseignements. Société Royale Belge de Géographie, 2(3), 577.

Skrzypek, E. (2011). Structural, petrological and geochronological contribution to intracontinental tectonics of the European Variscan Belt (Sudetes, Vosges Mts) [PhD Thesis]. Université de Strasbourg.

Staiger, J., Gosse, J., Little, E., Utting, D., Finkel, R., Johnson, J., & Fastook, J. (2006). Glacial erosion and sediment dispersion from detrital cosmogenic nuclide analyses of till. Quaternary Geochronology, 1(1), 29–42. https://doi.org/10.1016/j.quageo.2006.06.009

Stone, J. O. (2000). Air pressure and cosmogenic isotope production. Journal of Geophysical Research: Solid Earth, 105(B10), 753–759. https://doi.org/10.1029/2000JB900181

Strunk, A., Knudsen, M. F., Egholm, D. L., Jansen, J. D., Levy, L. B., Jacobsen, B. H., & Larsen, N. K. (2017). One million years of glaciation and denudation history in west Greenland. Nature Communications, 8(1), 14199. https://doi.org/10.1038/ncomms14199

Vermeesch, P. (2007). CosmoCalc: An Excel add-in for cosmogenic nuclide calculations. Geochemistry, Geophysics, Geosystems, 8(8). https://doi.org/10.1029/2006GC001530

Vidal, J.-P., Martin, E., Franchistéguy, L., Baillon, M., & Soubeyroux, J.-M. (2010). A 50-year high-resolution atmospheric reanalysis over France with the Safran system: A 50-year high-resolution atmospheric reanalysis over France. International Journal of Climatology, 30(11), 1627–1644. https://doi.org/10.1002/joc.2003 von Blanckenburg, F. (2005). The control mechanisms of erosion and weathering at basin scale from cosmogenic nuclides in river sediment. Earth and Planetary Science Letters, 237(3–4), 462–479. https://doi.org/10.1016/j.epsl.2005.06.030

Wittmann, H., Oelze, M., Gaillardet, J., Garzanti, E., & von Blanckenburg, F. (2020). A global rate of denudation from cosmogenic nuclides in the Earth's largest rivers. Earth-Science Reviews, 204, 103147. https://doi.org/10.1016/j.earscirev.2020.103147

Wittmann, H., von Blanckenburg, F., Guyot, J. L., Maurice, L., & Kubik, P. W. (2009). From source to sink: Preserving the cosmogenic 10Be-derived denudation rate signal of the Bolivian Andes in sediment of the Beni and Mamoré foreland basins. Earth and Planetary Science Letters, 288(3–4), 463–474. https://doi.org/10.1016/j.epsl.2009.10.008

Zhang, X., Cui, L., Xu, S., Liu, C., Zhao, Z., Zhang, M., & Liu- Zeng, J. (2021). Assessing non- steady-state erosion processes using paired 10Be– 26Al in southeastern Tibet. Earth Surface Processes and Landforms, 46(7), 1363–1374. https://doi.org/10.1002/esp.5105

Ziegler, P. A., & Dèzes, P. (2007). Cenozoic uplift of Variscan Massifs in the Alpine foreland: Timing and controlling mechanisms. Global and Planetary Change, 58(1–4), 237–269. https://doi.org/10.1016/j.gloplacha.2006.12.004

Figure1

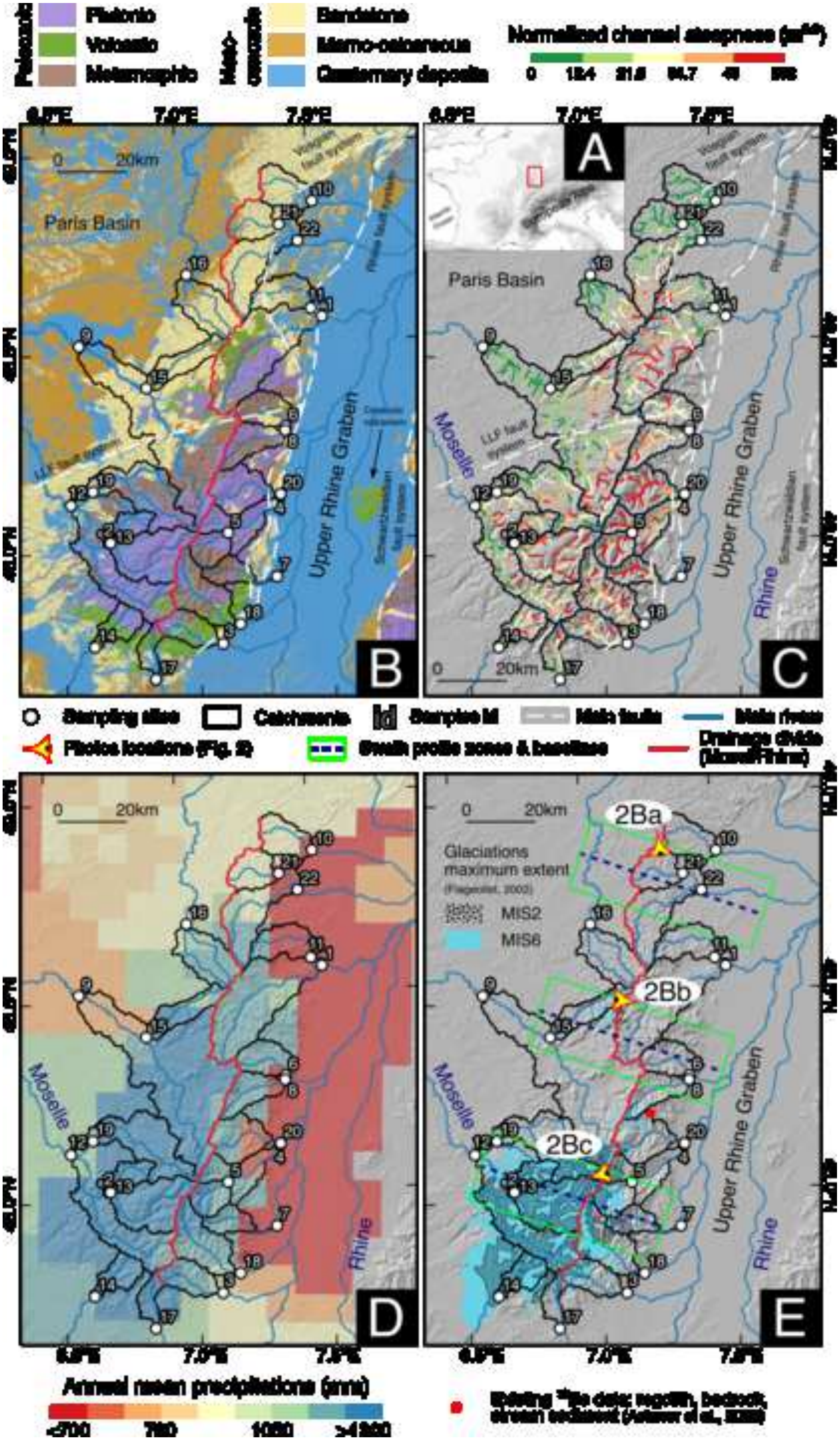
Paleozoic
Plutonic
Volcanic
Metamorphic
Meso-Cenozoic
Sandstone
Marno-calcareous
Quaternary deposits
Normalized channel steepness
0
12.4
21.8
34.7
48
A
B
C
D
E
0 20km
Paris Basin
Vosgian fault system
Rhine fault system
LLF fault system
Upper Rhine Graben
Schwarzwaldian fault system
Moselle
Rhine
Sampling sites
Catchments
Samples id
Main faults
Main rivers
Photos locations (Fig. 2)
Swath profile zones & baselines
Drainage divide (Moselle/Rhine)
2Ba
2Bb
2Bc
Glaciations maximum extent
(Flageollet, 2002)
MIS2
MIS6
Annual mean precipitations (mm)
<700
1050
>1200

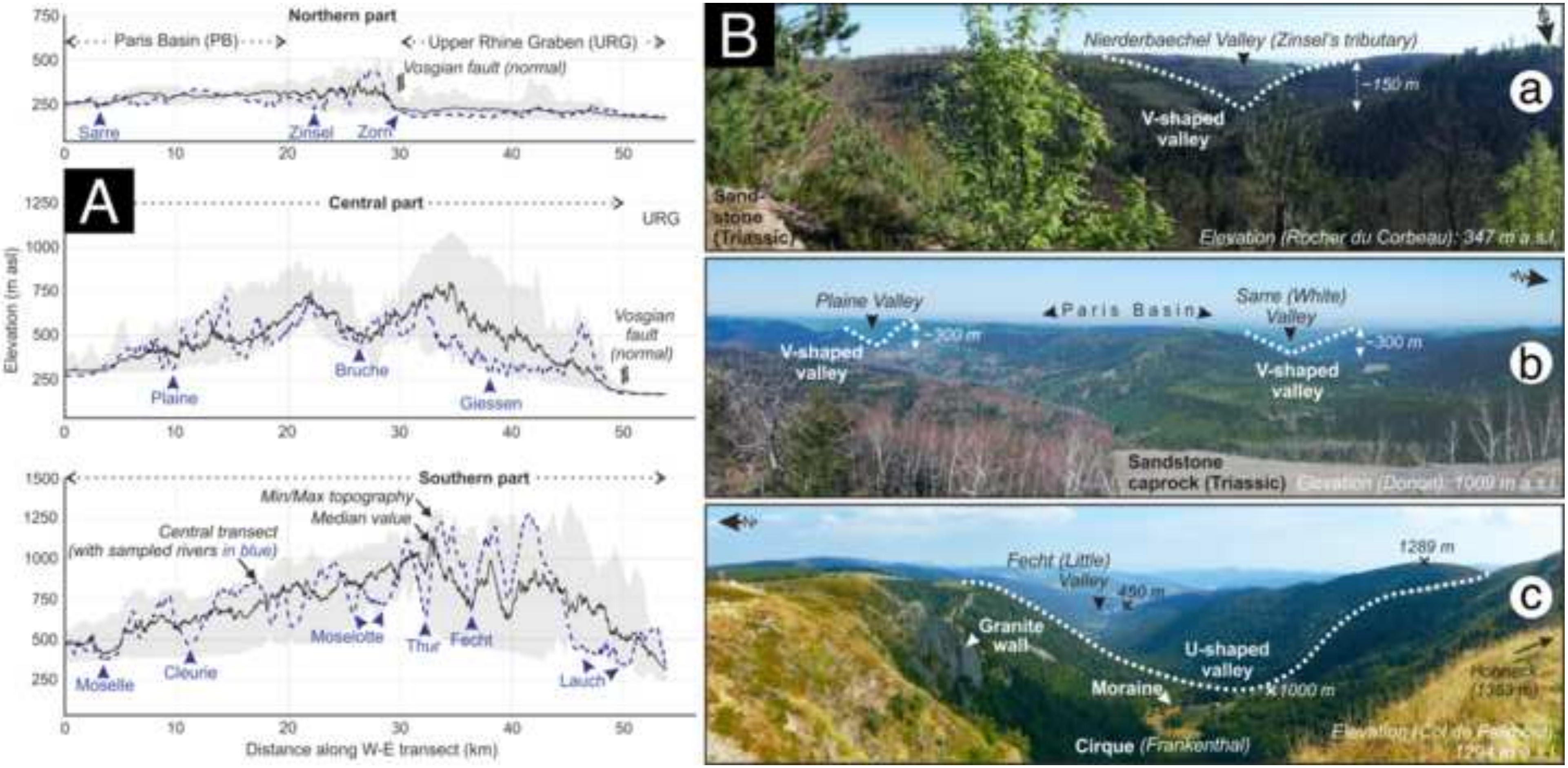
A
Northern part
Paris Basin (PB)
Upper Rhine Graben (URG)
Vosgian fault (normal)
Sarre
Zinsel
Zorn
Central part
URG
Vosgian fault (normal)
Plaine
Bruche
Giessen
Southern part
Min/Max topography
Median value
Central transect (with sampled rivers in blue)
Moselle
Cleurie
Moselotte
Thur
Fecht
Lauch
Elevation (m asl)
Distance along W-E transect (km)
0
10
20
30
40
50
250
500
750
1000
1250
1500
B
Nierderbaechel Valley (Zinsel's tributary)
~150 m
V-shaped valley
Sandstone (Triassic)
Elevation (Rocher du Corbeau): 347 m a.s.l.
a
Plaine Valley
Paris Basin
Sarre (White) Valley
~300 m
V-shaped valley
Sandstone caprock (Triassic)
Elevation (Donon): 1009 m a.s.l.
b
Fecht (Little) Valley
450 m
1289 m
Granite wall
U-shaped valley
Moraine
1000 m
Cirque (Frankenthal)
Hohneck (1363 m)
Elevation (Col de Falimont) 1294 m a.s.l.
c
N

Figure4

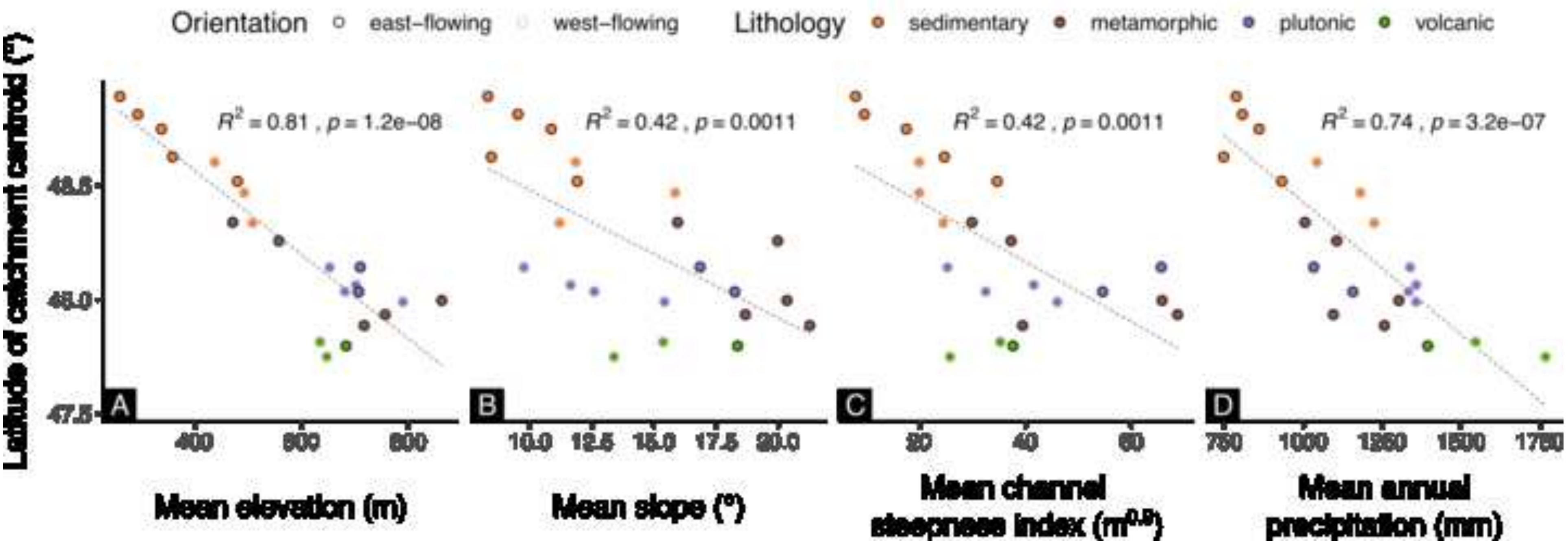
Orientation
east–flowing
west–flowing
Lithology
sedimentary
metamorphic
plutonic
volcanic
Latitude of catchment centroid (°)
48.5
48.0
47.5
A
$R^2 = 0.81$, $p = 1.2e-08$
400
600
800
Mean elevation (m)
B
$R^2 = 0.42$, $p = 0.0011$
10.0
12.5
15.0
17.5
20.0
Mean slope (°)
C
$R^2 = 0.42$, $p = 0.0011$
20
40
60
Mean channel steepness index ($m^{0.9}$)
D
$R^2 = 0.74$, $p = 3.2e-07$
750
1000
1250
1500
1750
Mean annual precipitation (mm)

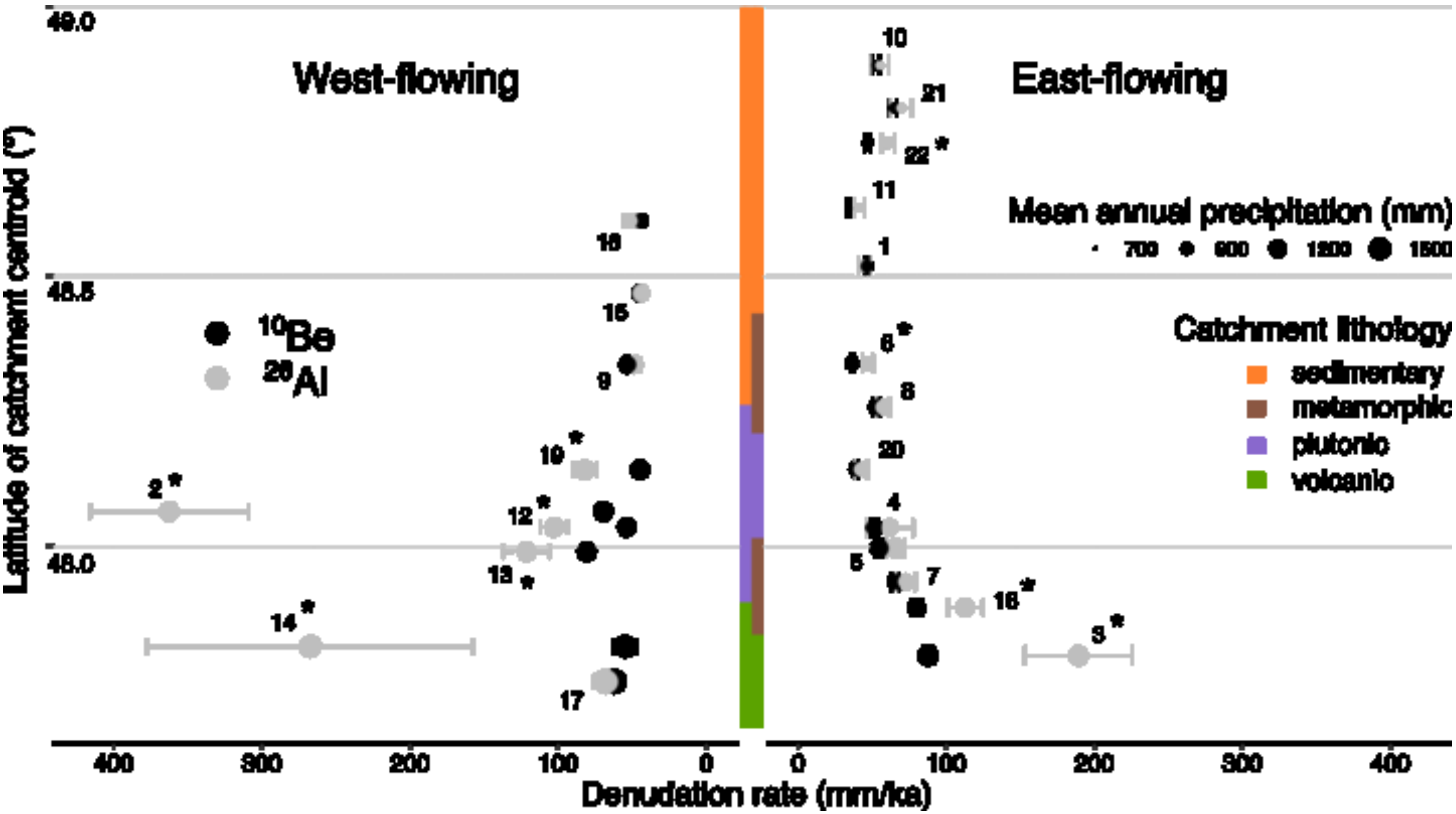
West-flowing
East-flowing
Latitude of catchment centroid (°)
49.0
48.5
48.0
^{10}Be
^{26}Al
Mean annual precipitation (mm)
700
900
1200
1500
Catchment lithology
sedimentary
metamorphic
plutonic
volcanic
10
21
22 *
11
1
6 *
8
20
4
5
7
16 *
3 *
18
15
9
19 *
2 *
12 *
13 *
14 *
17
400
300
200
100
0
Denudation rate (mm/ka)

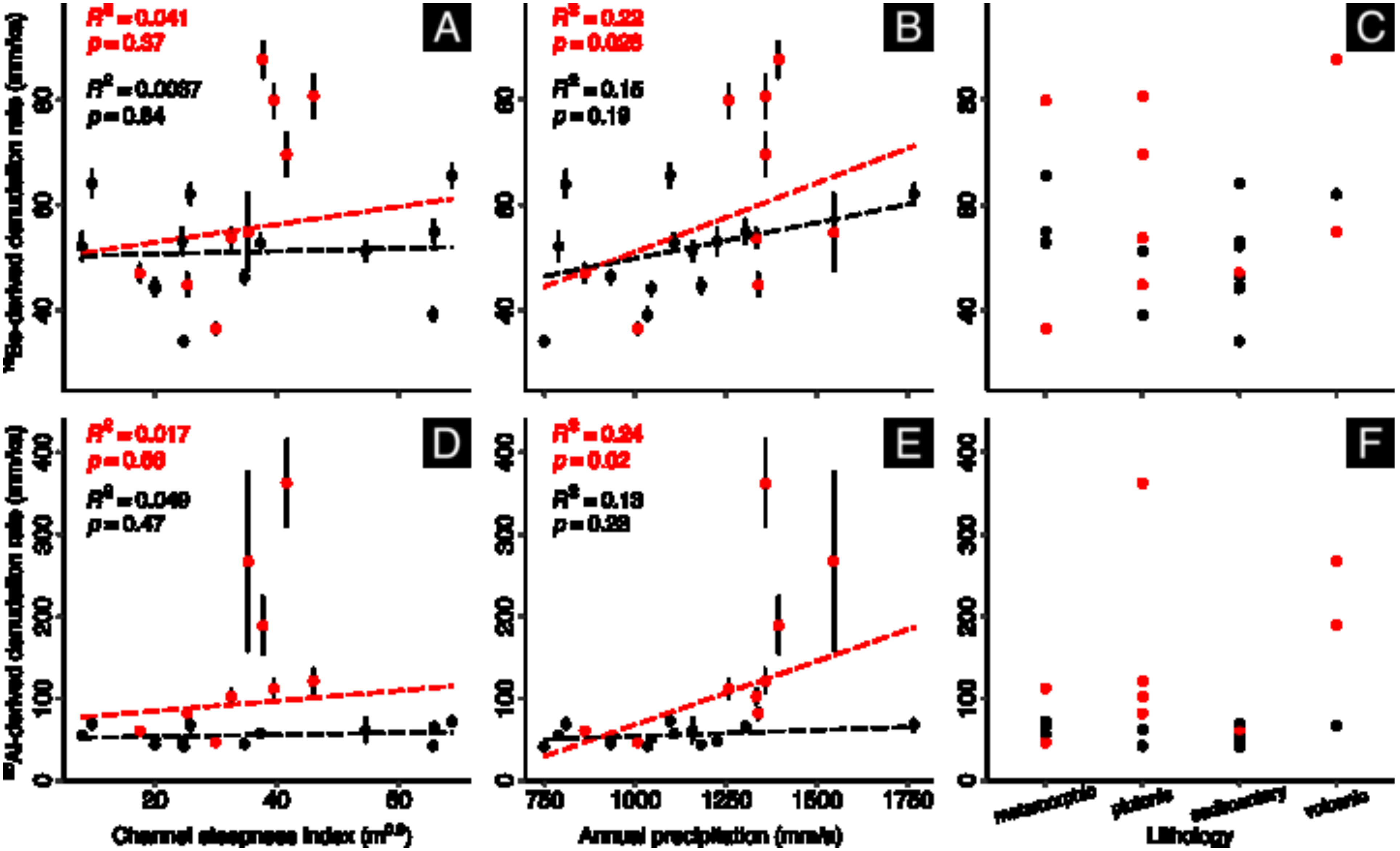
A
$R^2 = 0.041$
$p = 0.37$
$R^2 = 0.0067$
$p = 0.84$
B
$R^2 = 0.22$
$p = 0.026$
$R^2 = 0.15$
$p = 0.19$
C
D
$R^2 = 0.017$
$p = 0.66$
$R^2 = 0.049$
$p = 0.47$
E
$R^2 = 0.24$
$p = 0.02$
$R^2 = 0.13$
$p = 0.29$
F
^{10}Be-derived denudation rate (mm/ka)
^{26}Al-derived denudation rate (mm/ka)
40
60
80
0
100
200
300
400
20
40
60
Channel steepness index ($m^{0.9}$)
750
1000
1250
1500
1750
Annual precipitation (mm/a)
metamorphic
plutonic
sedimentary
volcanic
Lithology

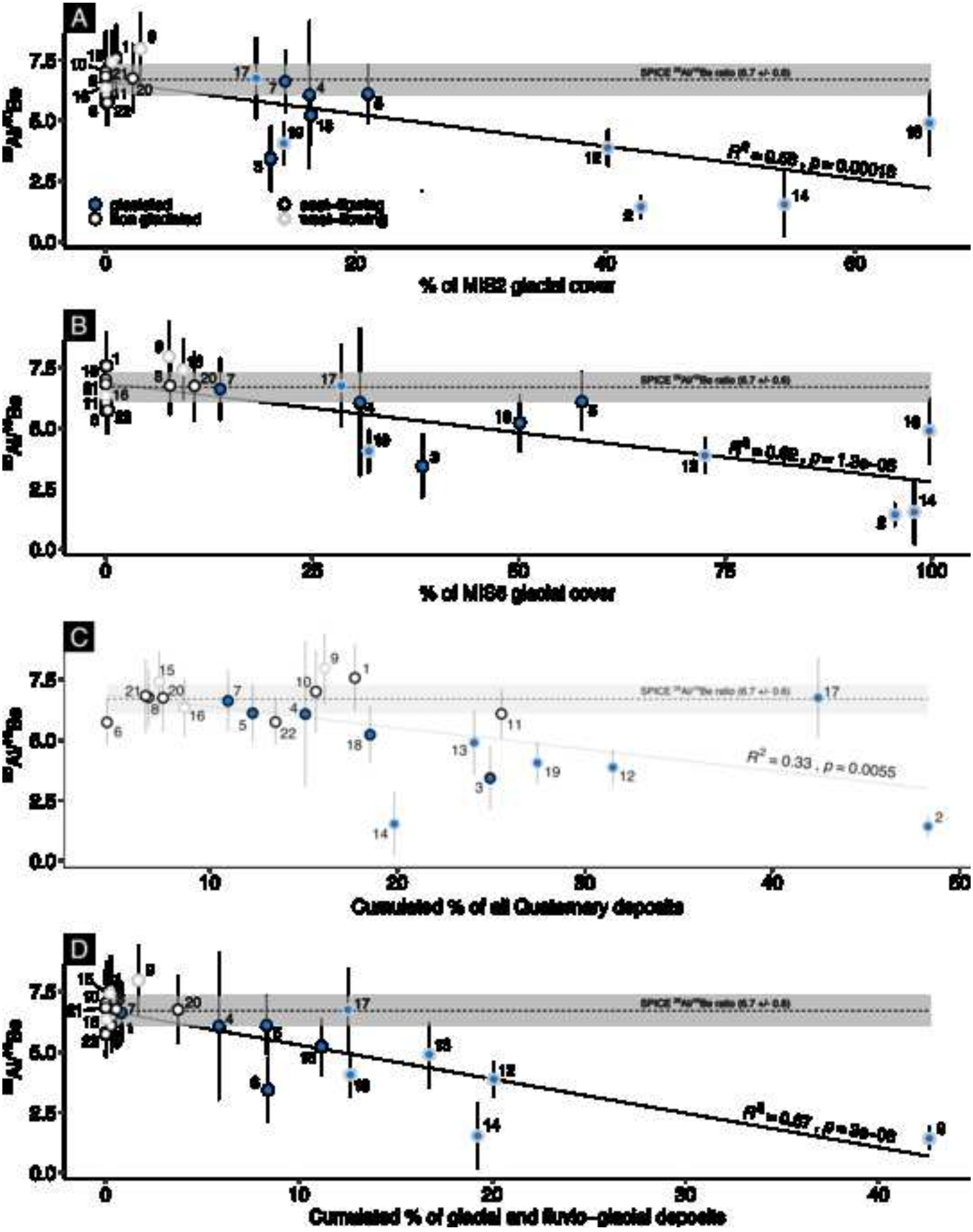
A
B
C
D
$^{26}Al/^{10}Be$
0.0
2.5
5.0
7.5
SPICE $^{26}Al/^{10}Be$ ratio (6.7 +/- 0.6)
glaciated
non glaciated
east-flowing
west-flowing
$R^2 = 0.58$, $p = 0.00018$
% of MIS2 glacial cover
0
20
40
60
$R^2 = 0.62$, $p = 1.3e-05$
% of MIS6 glacial cover
0
25
50
75
100
$R^2 = 0.33$, $p = 0.0055$
Cumulated % of all Quaternary deposits
10
20
30
40
50
$R^2 = 0.67$, $p = 3e-06$
Cumulated % of glacial and fluvio-glacial deposits
0
10
20
30
40

Figure9

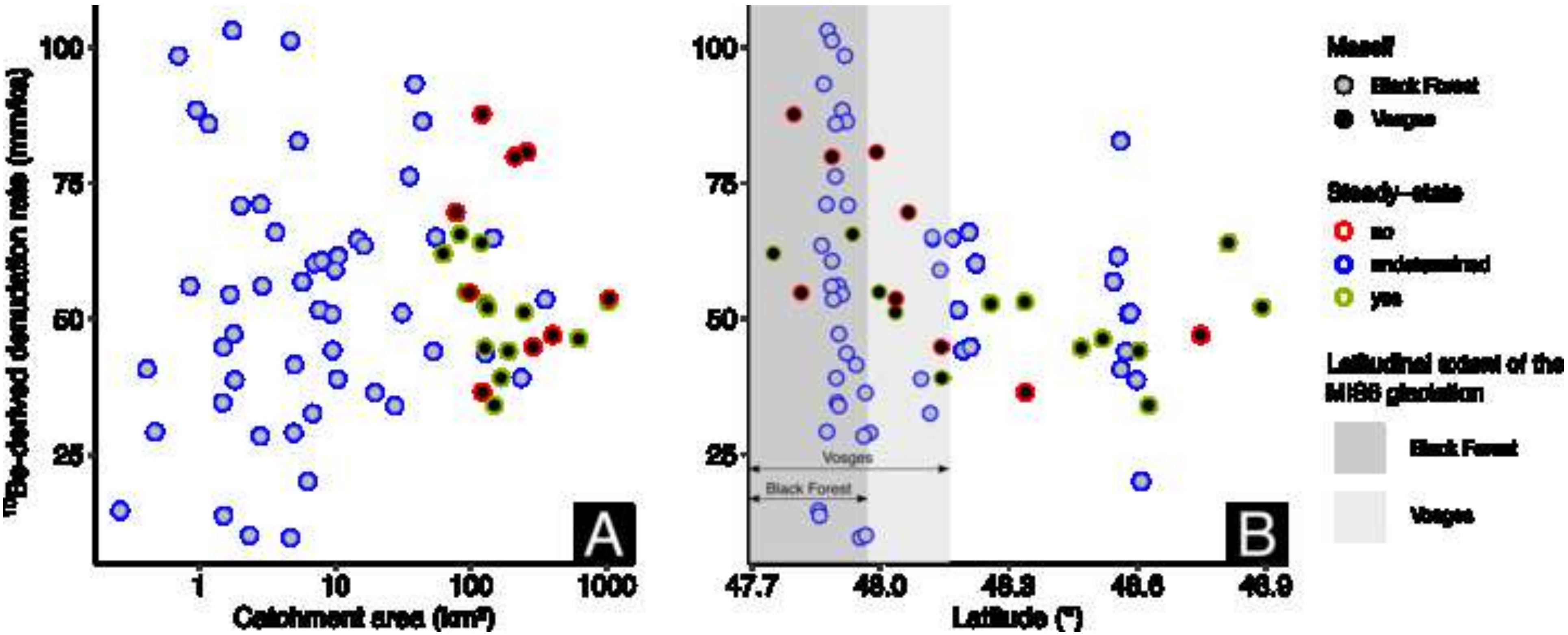
¹⁰Be-derived denudation rate (mm/ka)
100
75
50
25
1
10
100
1000
Catchment area (km²)
A
100
75
50
25
Vosges
Black Forest
47.7
48.0
48.3
48.6
48.9
Latitude (°)
B
Massif
Black Forest
Vosges
Steady-state
no
undetermined
yes
Latitudinal extent of the MIS6 glaciation
Black Forest
Vosges

Table 1: Sample location, catchment characteristics, and cosmogenic nuclide results based on ^{10}Be and ^{26}Al measurements in quartz from stream sediment. [a]Catchment area associated with sample location,determined from a 25-m resolution DEM (BD ALTI). [b]Mean elevation, [c]slope and [d]normalised channel steepness index (using the Mudd et al.'s (2018) LSD Topotools software with a reference concavity of 0.45) are all computed from the same DEM. [e]Mean annual precipitation determined from the national hydroclimatic database of Météo-France (Vidal et al., 2010) over the 1958-2009 period. [f]Glacial imprint based on the percentage of the catchment being ice-covered during MIS2 according to Flageollet (2002). >10% : yes; <10% : no. [g]Main lithology based on the hierarchical clustering analysis performed on bedrock lithologies and Quaternary deposits according to the same geological map (see Section 3.1). s: sedimentary, m: metamorphic, p: plutonic, v: volcanic. [h-i]Cosmogenic nuclide results for ^{10}Be and ^{26}Al.

Concentrations are corrected for a blank contribution. Analytical uncertainties (1σ) include both the AMS counting statistics and internal error (0.5% for ^{10}Be; Arnold et al., 2010), chemical blank measurement and ^{27}Al measurements. Denudation rates are inferred using CosmoCalc version 3.1 (Vermeesch, 2007), based on the time-independent Lal (1991)/Stone (2000) scaling model. We used a density of $2.7 g/cm^3$ and did not consider topographic shielding. Mean production rates were calculated from the latitude of the catchments centroids and their mean elevation[b]. Muonic productions were computed following Braucher et al. (2011). Reported uncertainties correspond to the 1σ analytical errors. Integration time corresponds to the time spent in the equivalent mean attenuation length (~60 cm).

[j]Minimum burial time assuming a simple burial scenario for *non-steady-state* samples, calculated using CosmoCalc version 3.1 (Vermeesch, 2007).

Figure 1: Main characteristics of the Vosges Mountains (VM) with sample locations for cosmogenic nuclide analysis and their associated catchments. A: Location of the VM in Central Europe, forming the southwestern uplifted flank of the Upper Rhine Graben. B: Simplified geological map (1/50.000) according to the French Geological Survey (BRGM). C: Normalized channel steepness index of the hydrological network calculated in the sampled catchments using LSD Topotools software (Mudd et al., 2018) with a reference concavity of 0.45. D: Annual mean precipitation from the national hydroclimatic database of Météo-France (Vidal et al., 2010) over the 1958-2009 period. E: Glaciation maximum extents of the supposedly Marine Isotope Stage (MIS)2 and MIS6 cold periods (Flageollet, 2002). Green rectangles and yellow eyes match the swath profiles and the field pictures of Fig. 2, respectively. The red point pinpoints already existing catchment-wide denudation rates in the VM (Ackerer et al., 2016, 2022).

Figure 2: (A) North-South topographic gradient of the VM from swath profiles and (B) associated landscapes (locations in Figure 1E).

Figure 3: Lithological surficial proportions of each sampled catchments according to the 1/50.000 BRGM geological map. Catchments are classified according to their centroid's latitude. Letters in brackets corresponds to the results of the hierarchical clustering analysis performed on the bedrock lithologies and Quaternary deposits (see Section 3.1): sedimentary (s), metamorphic (m), plutonic (p) and volcanic (v).

Figure 4: Significant relationships between the latitude of catchment centroids and the morphometric/ climatic factors in the VM. A: Mean elevation. B: Mean slope. C: Mean normalized channel steepness index. D: Mean annual precipitation. A second spatial gradient is also observed between the eastern-

and the western-flowing catchments. Note that statistics (R^2; p-value) are calculated using total least square regressions since the latitude does not depend on the controlling factors.

Figure 5: A: Two-nuclide diagram plotting ^{26}Al/^{10}Be ratios versus ^{10}Be concentrations. Sample ellipses correspond to 2σ analytical errors. Thirteen samples plot within the steady-erosion island and thus experienced steady-state erosion (grey ellipses). Nine samples plot below the steady-erosion island and thus experienced complex exposure histories (red ellipses). This plot was produced using CosmoCalc version 3.1 (Vermeesch, 2007), with the time-independent Lal (1991)/Stone (2000) scaling model. Muonic production was based on Braucher et al. (2011). B: Distribution of ^{26}Al-derived versus ^{10}Be-derived CWD rates. Error bars correspond to the 1σ analytical errors. Red and black points correspond to the *non-steady-state* and *steady-state catchments*, respectively (panel A). Note the logarithmic scales for both plots.

Figure 6: North-South distribution of CWD rates inferred from ^{10}Be (black points) and ^{26}Al (grey points) concentrations, along with the main lithologies and mean annual precipitation of the studied catchments. Horizontal error bars represent the 1σ uncertainty associated with the inferred CWD rates. *Non-steady-state catchments* are marked with an asterisk. The seven *non-steady-state samples* delivering the largest discrepancies in denudation values are all located in the southern part of the VM, regardless the catchment's lithology.

Figure 7: Relationships between CWD rates inferred from ^{10}Be (A-C) or ^{26}Al (D-F) concentrations and potential controlling factors: normalised channel steepness index, annual precipitation and main lithologies. (Red) black points correspond to the *(non)-steady-state samples*. Statistics are computed from linear regressions using the whole dataset (red lines) or the *steady-state* subset (black lines). A weak but significant relationship is observed between CWD rates and mean annual precipitation ($p\text{-value} < 0.03$). The significance of the relationship is lost when excluding the *non-steady-state samples* from the dataset (black lines).

Figure 8: Relationships between ^{26}Al/^{10}Be ratios and A: percentage of the catchment being ice-covered during MIS2, B: same for MIS6, C: cumulated percentage of all Quaternary deposits (i.e. alluvial, colluvial, glacial and fluvio-glacial deposits) and D: cumulated percentage of glacial and fluvio-glacial deposits. Glacial covers (A and B) are extracted from Flageollet's (2002) mapping. Quaternary sediment covers (C and D) are extracted from the BRGM's geological map. The vertical error bars correspond to the ^{26}Al/^{10}Be ratios at 1σ uncertainty. Blue points highlight the glaciated catchments (i.e. >10% of ice cover during MIS2). The horizontal dashed line corresponds to the surface production ratio recently determined by the SPICE project (6.7±0.6; Fenton et al., 2022). We did not use the surface production ratio from Cosmocalc (Vermeesch, 2007) as it does not provide any uncertainty. The strongest significant linear regression ($R^2 = 0.67$, p-value = 3e-06) is observed with the cumulated percentage of glacial and fluvio-glacial deposits (C).

Figure 9: Recalculated ^{10}Be-derived CWD rates in the Black Forest, compared to the ^{10}Be-derived CWD rates in the Vosges Massif, vs. A: catchment area and B: latitude of the catchment's centroid. The dark and light gray zones correspond to the latitudinal MIS6 glaciation extent of the Black Forest and the Vosges Massif, according to Flageollet (2002) and Ehlers et al. (2011), respectively.

Identification		**Sample location**		**Morphometric, climatic and lithological characteristics**					
River name	id	Latitude (°)	Longitude (°)	Area^a (km²)	Mean elevation^b (m)	Mean slope^c (°)	Mean $k_{sn}{}^d$ ($m^{0.9}$)	Mean annual precipitation^e (mm)	Glacial imprint^f
Bruche	1	48.57	7.53	622.0	480.0	11.9	34.7	931.7	no
Cleurie	2	48.02	6.68	77.5	701.5	11.6	41.6	1357.6	yes
Doller	3	47.76	7.09	120.8	683.3	18.4	37.7	1394.2	yes
Fecht	4	48.12	7.33	246.0	707.1	18.2	54.6	1157.3	yes
Fecht	5	48.04	7.13	91.4	862.4	20.4	65.8	1302.8	yes
Giessen	6	48.30	7.36	121.4	471.3	15.9	29.9	1005.4	no
Lauch	7	47.92	7.30	83.1	756.6	18.7	68.7	1095.2	yes
Liepvrette	8	48.28	7.36	127.8	557.6	20.0	37.3	1105.8	no
Meurthe	9	48.52	6.60	1035.0	508.4	11.2	24.5	1224.5	no
Moder	10	48.86	7.51	132.4	260.2	8.3	8.0	788.0	no
Mossig	11	48.59	7.48	148.8	358.8	8.4	24.7	747.8	no
Moselle	12	48.12	6.54	1037.0	681.0	12.6	32.5	1333.3	yes
Moselotte	13	48.02	6.69	258.4	789.7	15.4	46.0	1357.0	yes
Ognon	14	47.76	6.61	96.9	634.8	15.4	35.3	1545.6	yes
Plaine	15	48.41	6.85	126.8	492.5	15.8	20.0	1180.7	no
Sarre	16	48.69	7.02	188.8	437.4	11.8	20.0	1043.7	no
Savoureuse	17	47.68	6.83	62.4	647.2	13.4	25.8	1766.9	yes
Thur	18	47.80	7.16	210.6	717.1	21.3	39.5	1256.8	yes
Vologne	19	48.15	6.63	286.8	652.6	9.7	25.3	1338.1	yes
Weiss	20	48.13	7.33	166.1	709.7	16.9	65.6	1033.0	no
Zinsel du Sud	21	48.80	7.38	119.8	293.7	9.5	9.6	807.4	no
Zorn	22	48.76	7.45	400.5	337.9	10.8	17.5	860.1	no

plain_text_2

	^{10}Be results[h]			**^{26}Al results**[i]			
Main lithology[g]	[^{10}Be] 10^4 (at/g) qtz	^{10}Be - denudation rate (mm/ka)	^{10}Be - integration time (ka)	[^{26}Al] 10^4 (at/g) qtz	^{26}Al - denudation rate (mm/ka)	^{26}Al - integration time (ka)	^{26}Al/^{10}Be
s	9.8 +/- 0.3	46 +/- 1	13.0	74 +/- 6	45 +/- 4	13.4	7.6 +/- 0.7
p	7.7 +/- 0.5	70 +/- 4	8.6	11.1 +/- 2	363 +/- 53	1.7	1.4 +/- 0.2
v	6.1 +/- 0.2	88 +/- 4	6.8	20.8 +/- 4	189 +/- 36	3.2	3.4 +/- 0.7
p	10.5 +/- 0.4	51 +/- 2	11.7	63.8 +/- 16	62 +/- 16	9.7	6.1 +/- 1.5
m	11 +/- 0.5	55 +/- 2	10.9	67.3 +/- 6	66 +/- 6	9.1	6.1 +/- 0.6
m	12.2 +/- 0.4	36 +/- 1	16.5	70.2 +/- 5	47 +/- 4	12.8	5.7 +/- 0.5
m	8.5 +/- 0.3	66 +/- 2	9.1	56.5 +/- 5	73 +/- 7	8.3	6.6 +/- 0.6
m	9.1 +/- 0.3	53 +/- 2	11.4	61.6 +/- 5	57 +/- 5	10.5	6.8 +/- 0.6
s	8.7 +/- 0.4	53 +/- 3	11.3	69.5 +/- 5	49 +/- 4	12.3	8 +/- 0.7
s	7.3 +/- 0.4	52 +/- 3	11.5	51.5 +/- 6	55 +/- 6	10.9	7 +/- 0.9
s	12 +/- 0.4	34 +/- 1	17.6	73 +/- 6	41 +/- 3	14.5	6.1 +/- 0.5
p	9.8 +/- 0.3	54 +/- 2	11.2	38.1 +/- 3	103 +/- 9	5.8	3.9 +/- 0.4
p	7.1 +/- 0.4	81 +/- 4	7.4	34.9 +/- 4	121 +/- 16	4.9	4.9 +/- 0.7
v	9.3 +/- 1.3	55 +/- 8	11.0	14.2 +/- 6	267 +/- 110	2.2	1.5 +/- 0.7
s	10.2 +/- 0.3	45 +/- 2	13.4	75.9 +/- 6	44 +/- 4	13.6	7.4 +/- 0.6
s	9.9 +/- 0.3	44 +/- 1	13.6	63 +/- 6	51 +/- 5	11.7	6.3 +/- 0.6
v	8.3 +/- 0.3	62 +/- 2	9.7	55.9 +/- 7	67 +/- 8	8.9	6.8 +/- 0.8
m	6.8 +/- 0.3	80 +/- 3	7.5	35.6 +/- 4	113 +/- 12	5.3	5.2 +/- 0.6
p	11.5 +/- 0.6	45 +/- 2	13.4	46.6 +/- 4	82 +/- 8	7.3	4.1 +/- 0.4
p	13.7 +/- 0.5	39 +/- 1	15.3	92.5 +/- 9	42 +/- 4	14.2	6.7 +/- 0.7
s	6.2 +/- 0.2	64 +/- 3	9.4	42.1 +/- 4	69 +/- 7	8.7	6.8 +/- 0.8
s	8.6 +/- 0.3	47 +/- 2	12.8	49.7 +/- 4	61 +/- 4	9.9	5.7 +/- 0.5

Minimum burial time[j] (ka)
3351.3
1570.7
501.2
1310.3
832.5
3198.7
701.4
1210.6
508.7

Identification		Sample location		Morphometric, climatic and lithological characteristics					
River name	id	Latitude (°)	Longitude (°)	Area[a] (km²)	Mean elevation[b] (m)	Mean slope[c] (°)	Mean k_{sn}[d] ($m^{0.9}$)	Mean annual precipitations[e] (mm)	Glacial imprint[f]
Bruche	1	48.57	7.53	622.0	480.0	11.9	34.7	931.7	no
Cleurie	2	48.02	6.68	77.5	701.5	11.6	41.6	1357.6	yes
Doller	3	47.76	7.09	120.8	683.3	18.4	37.7	1394.2	yes
Fecht	4	48.12	7.33	246.0	707.1	18.2	54.6	1157.3	yes
Fecht	5	48.04	7.13	91.4	862.4	20.4	65.8	1302.8	yes
Giessen	6	48.30	7.36	121.4	471.3	15.9	29.9	1005.4	no
Lauch	7	47.92	7.30	83.1	756.6	18.7	68.7	1095.2	no
Liepvrette	8	48.28	7.36	127.8	557.6	20.0	37.3	1105.8	no
Meurthe	9	48.52	6.60	1035.0	508.4	11.2	24.5	1224.5	no
Moder	10	48.86	7.51	132.4	260.2	8.3	8.0	788.0	no
Mossig	11	48.59	7.48	148.8	358.8	8.4	24.7	747.8	no
Moselle	12	48.12	6.54	1037.0	681.0	12.6	32.5	1333.3	yes
Moselotte	13	48.02	6.69	258.4	789.7	15.4	46.0	1357.0	yes
Ognon	14	47.76	6.61	96.9	634.8	15.4	35.3	1545.6	yes
Plaine	15	48.41	6.85	126.8	492.5	15.8	20.0	1180.7	no
Sarre	16	48.69	7.02	188.8	437.4	11.8	20.0	1043.7	no
Savoureuse	17	47.68	6.83	62.4	647.2	13.4	25.8	1766.9	yes
Thur	18	47.80	7.16	210.6	717.1	21.3	39.5	1256.8	yes
Vologne	19	48.15	6.63	286.8	652.6	9.7	25.3	1338.1	yes
Weiss	20	48.13	7.33	166.1	709.7	16.9	65.6	1033.0	no
Zinsel du Sud	21	48.80	7.38	119.8	293.7	9.5	9.6	807.4	no
Zorn	22	48.76	7.45	400.5	337.9	10.8	17.5	860.1	no

	^{10}Be results[h]			**^{26}Al results**[i]			
Main lithology[g]	[^{10}Be] 10^4 (at/g) qtz	^{10}Be - denudation rate (mm/ka)	^{10}Be - integration time (ka)	[^{26}Al] 10^4 (at/g) qtz	^{26}Al - denudation rate (mm/ka)	^{26}Al - integration time (ka)	^{26}Al/^{10}Be
s	9.8 +/- 0.3	46 +/- 1	13.0	74 +/- 6	45 +/- 4	13.4	7.6 +/- 0.7
p	7.7 +/- 0.5	70 +/- 4	8.6	11.1 +/- 2	363 +/- 53	1.7	1.4 +/- 0.2
v	6.1 +/- 0.2	88 +/- 4	6.8	20.8 +/- 4	189 +/- 36	3.2	3.4 +/- 0.7
p	10.5 +/- 0.4	51 +/- 2	11.7	63.8 +/- 16	62 +/- 16	9.7	6.1 +/- 1.5
m	11 +/- 0.5	55 +/- 2	10.9	67.3 +/- 6	66 +/- 6	9.1	6.1 +/- 0.6
m	12.2 +/- 0.4	36 +/- 1	16.5	70.2 +/- 5	47 +/- 4	12.8	5.7 +/- 0.5
m	8.5 +/- 0.3	66 +/- 2	9.1	56.5 +/- 5	73 +/- 7	8.3	6.6 +/- 0.6
m	9.1 +/- 0.3	53 +/- 2	11.4	61.6 +/- 5	57 +/- 5	10.5	6.8 +/- 0.6
s	8.7 +/- 0.4	53 +/- 3	11.3	69.5 +/- 5	49 +/- 4	12.3	8 +/- 0.7
s	7.3 +/- 0.4	52 +/- 3	11.5	51.5 +/- 6	55 +/- 6	10.9	7 +/- 0.9
s	12 +/- 0.4	34 +/- 1	17.6	73 +/- 6	41 +/- 3	14.5	6.1 +/- 0.5
p	9.8 +/- 0.3	54 +/- 2	11.2	38.1 +/- 3	103 +/- 9	5.8	3.9 +/- 0.4
p	7.1 +/- 0.4	81 +/- 4	7.4	34.9 +/- 4	121 +/- 16	4.9	4.9 +/- 0.7
v	9.3 +/- 1.3	55 +/- 8	11.0	14.2 +/- 6	267 +/- 110	2.2	1.5 +/- 0.7
s	10.2 +/- 0.3	45 +/- 2	13.4	75.9 +/- 6	44 +/- 4	13.6	7.4 +/- 0.6
s	9.9 +/- 0.3	44 +/- 1	13.6	63 +/- 6	51 +/- 5	11.7	6.3 +/- 0.6
v	8.3 +/- 0.3	62 +/- 2	9.7	55.9 +/- 7	67 +/- 8	8.9	6.8 +/- 0.8
m	6.8 +/- 0.3	80 +/- 3	7.5	35.6 +/- 4	113 +/- 12	5.3	5.2 +/- 0.6
p	11.5 +/- 0.6	45 +/- 2	13.4	46.6 +/- 4	82 +/- 8	7.3	4.1 +/- 0.4
p	13.7 +/- 0.5	39 +/- 1	15.3	92.5 +/- 9	42 +/- 4	14.2	6.7 +/- 0.7
s	6.2 +/- 0.2	64 +/- 3	9.4	42.1 +/- 4	69 +/- 7	8.7	6.8 +/- 0.8
s	8.6 +/- 0.3	47 +/- 2	12.8	49.7 +/- 4	61 +/- 4	9.9	5.7 +/- 0.5

Minimum burial time (ka)	Burial-corrected denudation rate (mm/ka)	Minimum burial time (ka)	Burial-corrected denudation rate (mm/ka)	error
3351.3	12 +/- 6	3351.3	12.4	6.0
1570.7	39 +/- 54	1570.7	39.4	53.7
501.2	28 +/- 25	501.2	28.1	25.0
1310.3	27 +/- 20	1310.3	27.4	19.9
832.5	53 +/- 69	832.5	52.9	69.3
3198.7	10 +/- 15	3198.7	10.4	14.7
701.4	56 +/- 64	701.4	55.9	64.1
1210.6	24 +/- 20	1210.6	24.0	19.6
508.7	36 +/- 31	508.7	36.2	31.2

Table_S1

Table_S2

Declaration of Interest Statement

The authors declare that they have no known competing financial interests or personal relationships that could have appeared to influence the work reported in this paper.